UNIVERSITY OF CAPE TOWN
Department of Mechanical Engineering
Rondebosch, Cape Town, South Africa

BLAST IMPACT AND SURVIVABILITY RESEARCH UNIT

BISRU

The effects of blast induced imperfections on the energy absorption characteristics of square tubes

Steeve Chung Kim Yuen

SEPTEMBER 2006

Thesis presented for the degree of Doctor of Philosophy in Engineering in the Department of Mechanical Engineering, University of Cape Town.

Declaration

I, Steeve Chung Kim Yuen, hereby:

(a) grant the University free license to reproduce this thesis, entitled "The effects of blast-induced imperfections on the energy absorption characteristics of square tubes", in whole or in part, for the purpose of research;

(b) declare that:

(i) this thesis is my own unaided work, both in conception and execution, and that apart from the normal guidance of my supervisor, I have received no assistance apart from that stated in the "acknowledgement" section;

(ii) this thesis or any part of this thesis has not been submitted in past, or is being, or is to be submitted in this or any other form for a degree at the University or any other University.

(iii) I am now presenting this thesis for examination for the Degree of PhD

.....

Steeve Chung Kim Yuen

September 2006

Abstract

The geometric deformation induced by two equal blast loads on opposite sides of a thin-walled square tube will weaken the structure. This will improve its energy absorbtion characteristics compared to a geometrically "perfect" square tube of the same size by reducing the crush load when compressed in the axial direction. Different types of imperfection can be induced depending on the size of the blast loads.

Consequent to the blast loads, high temperatures will also be induced by adiabatic heating due to large plastic deformation and high strain rate. It is expected that the material properties of the tube will be affected in the region of the imperfections. It is anticipated that the temperature will have a greater effect than the strain rate in that the material properties of the tube in the region of the blast will soften (increase in temperature causes yield stress to decrease while an increase in strain rate causes yield stress to increase).

This investigation examines how blast-induced imperfections at opposite sides of a square tube affect the thin-wall structure and reduce its crush load when compressed in the axial direction i.e. its energy absorption characteristics. A series of experimental results and numerical simulations using the hydro-dynamic code; AutoDYN, to characterise the blast load, and finite element package; ABAQUS/*Explicit* v6.5-6, to predict the response of the mild steel tubes, are reported.

Blast imperfections are induced in the square tubes on opposite sides with the use of plastic explosive (PE4). The explosive, in disc shape, is placed at mid length of mild steel square tubes, of two cross-sections 50x50x1.5mm and 75x75x1.6mm. The blast loads provide the impulse required to create geometric changes and affect the material properties of the tubes.

Three geometric changes occur in the mid-section of the tubes and are classified as:-

- large inelastic deformation of the tube sides without contacting each other
- large inelastic deformation of the tube sides contacting and rebounding off each other
- large inelastic deformation of the tube sides with a disc-shape fragment blown out at the centre

The tubes, with the blast-induced imperfections, are thereafter loaded in axial direction, quasi-statically or dynamically. These results are compared to those obtained for square tubes with no imperfections and circular holes with a view to investigate the effects of the geometric and material property changes on the energy absorption characteristics of the tube. Results obtained from the quasi-static tests show that the introduction of the blast-induced imperfections does not change the buckling mode of the tube but reduces the crush force. The buckling modes obtained from the dynamic tests are similar to the quasi-static tests.

For the numerical simulation, the blast load is characterised using the hydro-dynamic code AutoDYN which allows the interaction of Euler and Lagrangian meshes and then modelled by means of a pressure pulse. The dynamic-explicit finite element code; ABAQUS/*Explicit* v6.5-6 which incorporates non-linear geometry, material effects such as strain rate sensitivity and temperature is used to simulate both the large inelastic deformation and tearing mode of the square tube due to the blast loads and the buckling mode of the square tube due to the dynamic impact load. A half symmetry model with eight noded brick hourglass control continuum elements (C3D8R) and shell elements (S4R) both with reduced integration is used.

The predicted tube responses to the localised blast loading; maximum deflection of the tube side and tearing are compared to the experimental results. High temperatures and severe element elongations due to very high strain in localised area indicates where tearing is most likely to take place.

For the dynamic axial loading, the predicted tube response is compared for crushed shape; number of lobes formed and crushed distance. The force-displacement data obtained from the finite element model is used to asses the effects of the imperfections on the energy absorption characteristics of the tube.

The numerical prediction compares well with experimental data for both the blast loading and the dynamic axial loading.

Conclusions drawn are that the blast-induced imperfections reduce the crush force but do not change the buckling mode. The geometry changes as a result of the blast-induced imperfections have a greater influence on the energy absorption characteristics of the tube than the changes in material properties. The tubes with the non-touching domes crush with lower crush forces than tubes with rebound domes.

For the dynamic axial loading, the predicted tube response is compared for crushed shape; number of lobes formed and crushed distance. The force-displacement data obtained from the finite element model is used to asses the effects of the imperfections on the energy absorption characteristics of the tube.

The numerical prediction compares well with experimental data for both the blast loading and the dynamic axial loading.

Conclusions drawn are that the blast-induced imperfections reduce the crush force but do not change the buckling mode. The geometry changes as a result of the blast-induced imperfections have a greater influence on the energy absorption characteristics of the tube than the changes in material properties. The tubes with the non-touching domes crush with lower crush forces than tubes with rebound domes.

Table of Contents

Declaration i
Abstract iii
Table of Contents vii
List of Figures xv
List of Tables xxix
Nomenclature xxxi
Acknowledgement xxxv

1.0 Introduction 1

2.0 Literature Review on Tube Crushing 7

2.1 Experimental studies 8
2.1.1 Modes of buckling 8
2.1.1.1 Euler buckling 9
2.1.1.2 Progressive buckling 10
2.1.1.3 Dynamic plastic buckling 14
2.1.2 The effects of the geometry of the tube 15
2.1.2.1 Influence of tube length on collapse mode 15
2.1.2.2 Effect of thickness/ width ratio 20
2.1.3 Effect of material properties 21
2.1.4 Geometric imperfections 22
2.1.4.1 Pre-buckle 23
2.1.4.2 Sharp corner indentations 24
2.1.4.3 Parallel indentations in the side of the tubes 25
2.1.4.4 Circular cut-outs 33
2.1.4.5 Combined structural deformations 36
2.1.4.6 Stiffened tubes 38
2.1.4.7 Foam-filled tubes 40
2.1.4.8 Wrapped tubes 46
2.2 Theoretical analysis 50

2.2.1 Buckling load 52
2.2.1.1 The mean static buckling load *52*
2.2.1.2 Effective crushing distance *54*
2.2.1.3 The mean dynamic buckling load *55*
2.2.1.4 Ultimate buckling load *58*
2.2.2 Energy absorption of the structures 59
2.2.2.1 Geometric efficiency, e_C *59*
2.2.2.2 Load efficiency, e_l *60*
2.2.2.3 Energy efficiency, e_E *60*
2.2.2.4 Specific energy, S *60*
2.3 Computational predictions 61
2.3.1 Influence of the impact mass 67
2.3.2 Influence of the impact velocity 68
2.3.3 Transition in buckling mode 69
2.3.4 Geometric Imperfections 71
2.3.5 Foam-filled tubes 72
2.3.6 Composite tubes 72
2.3.7 Compound tubes 73
2.3.8 Optimisation 73
2.3.9 Fracture model 75

3.0 Literature Review on Blast Loading 79

3.1 Blast loads 79
3.1.1 Idealised blast pressure time history 81
3.1.2 Blast loading conditions 83
3.2 Experimental studies 89
3.2.1 Modes of failure 89
3.2.2 Structural response 91
3.2.2.1 Uniform blast load *91*
3.2.2.1 Localised blast load *95*
3.2.3 The effect of boundary conditions on failure 97
3.3 Theoretical predictions 100
3.4 Predictions of structural response 104

4.0 Experimental Details 113

4.1 Test specimens 114
Tensile testing 114
4.2 Blast loading of tubes 117
4.2.1 Ballistic pendulum 117
4.2.2 Explosive load geometry and material properties 119
4.3 Quasi-static axial loading of tubes 120
4.4 Dynamic axial loading of tubes 121
4.5 Combined blast and dynamic axial loading 123

5.0 Experimental Results 125

5.1 Blast loading 125
5.1.1 Blast response of 50mm square tubes 126
Load diameter 17mm 126
Load diameter 25mm 128
5.1.2 Blast response of 75mm square tubes 129
Load diameter 25mm 129
Load diameter 37.5mm 130
5.1.3 Summary of tube response 131
5.2 Quasi-static axial loading 134
5.2.1 Geometrically "perfect" square tubes 134
5.2.2 Square tubes with circular cut-outs 135
5.2.3 Square tubes with simple Mode I imperfections 137
5.2.4 Square tubes with rebound imperfections 139
5.2.5 Square tubes with capping imperfections 141
5.3 Dynamic axial loading 146
5.3.1 Geometrically "perfect" 50mm square tubes 146
5.3.2 Geometrically "perfect" 75mm square tubes 149
5.3.3 50mm square tubes with circular cut-outs 150
5.3.4 Discussions 152
5.4 Combined loading 154
5.4.1 Simple Mode I imperfections 154
50mm square tube 154

75mm square tube *155*
5.4.2 Rebound imperfections 157
5.4.3 Capping imperfections 158
50mm square tube *158*
5.4.4 Asymmetric imperfections 159
50mm square tube *159*
75mm square tube *161*
5.4.5 Discussions 162
50mm square tube *162*
75mm square tube *163*

6.0 Analysis of Experimental Results 165

6.1 Blast loading 165
6.1.1 Relationship between explosive mass and impulse 167
6.1.2 Relationship between tube deflection and impulse 169
6.2 Quasi-static axial loading 170
6.2.1 As received square tubes 170
Mean static crushing load *171*
Ultimate buckling load *172*
6.2.2 Induced geometric imperfection square tubes 173
Mean crushing load *178*
Ultimate buckling load *179*
Load efficiency, ec *180*
6.2.3 The effect of heat treatment on tube crushing 181
6.3 Dynamic axial loading 182
6.3.1 Geometrically "perfect" tubes 183
6.3.2 Tubes with circular cut-out imperfections 186
6.3.3 Tubes with blast-induced simple Mode 1 imperfections 187
6.3.4 Tubes with blast-induced rebound imperfections 188
6.3.5 Tubes with blast-induced cap imperfections 189
6.3.6 Axial crushing of n number of square tubes, [44] 190
Geometric efficiency, ec *194*
6.4 Influence of dynamic axial loading 197

7.0 Finite Element Formulation 199

7.1 Finite Element analysis method 199
7.2 Geometrical modelling of the square tube 201
7.2.1 Types of elements used in the finite element model 201
Continuum C3D8R element 201
Shell S4R element 202
7.2.2 Meshing the finite element model 202
7.3 Material properties of the square tube 204
7.3.1 Johnson-Cook plasticity model 205
7.3.2 Classical metal plasticity model 206
7.3.2.1 Yield hardening 206
7.3.2.2 Strain rate dependence 208
7.3.2.3 Temperature dependence 208
7.3.2.4 Strain based shear failure criteria 211
7.4 Boundary conditions 212
7.5 Contacts 213
7.6 Blast load modelling 213
7.7 Dynamic axial load modelling 219
7.8 Combined loading 220

8.0 Finite Element Simulation Results 221

8.1 Blast loading 221
8.1.1 Establishing simulation time 221
8.1.2 Simple Mode I response 223
8.1.2.1 50mm square tube, load diameter 17mm 223
8.1.2.2 50mm square tube, load diameter 25mm 225
8.1.2.3 75mm square tube 226
8.1.3 Rebound response 228
8.1.2.3 Overall comparison 229
8.1.4 Capping (Mode IIc) 230
8.1.4.1 Failure Mechanism 231
8.1.4.2 Predicting tearing of 50mm tube 232
8.1.4.3 Predicting tearing of 75mm tube 233

8.2 Dynamic axial loading 236
8.2.1 "Perfect" 50mm square tubes 237
8.2.2 "Perfect" 75mm square tube 238
8.2.3 50mm square tube with circular cut-outs 239
8.3 Combined loading 243
8.3.1 Simple Mode I imperfections 244
8.3.1.1 50mm square tube subjected to blast load diameter 17mm 244
9.3.1.2 75mm square tube subjected to blast load diameter 37.5mm 248
8.3.2 Rebound imperfections 252
8.3.2.1 50mm square tube subjected to blast load diameter 17mm 252
8.3.2.2 50mm square tube subjected to blast load diameter 25mm 256
8.3.3 Capping imperfections 258
8.3.3.1 50mm square tube subjected to blast load diameter 17mm 258

9.0 Discussion of Finite Element Results 265

9.1 The influence of asymmetric blast-induced imperfections 266
9.2 The influence of drop masses 271
9.3 The influence of impact velocities 273
9.4 The combined influence of drop mass and impact velocity 275
9.5 The influence of circular cut-out imperfections 277
9.6 The influence of blast-induced imperfections 280
9.6.1 The influence of material property change 280
9.6.2 The influence of impulse and load diameter – 50mm tube 283
9.6.2.1 Blast-induced imperfection type 283
9.6.2.2 Predicted collapse mode 285
9.6.3 The influence of impulse and load diameter – 75mm tube 288
9.6.3.1 Blast-induced imperfection type 288
9.6.3.2 Predicted collapse mode 290
9.6.4 The influence of tube width on response 293
9.6.4.1 Blast response 293
9.6.4.2 Crushing behaviour 293

10.0 Conclusions 297

Blast loading 299
Combined loading 300
Influence of changes in material properties 300
Influence of imperfection types 301
Simple Mode I imperfections 301
Rebound and capping imperfections 301
Folding mechanisms 302

11.0 Recommendations 303

12.0 References 305

Appendix A - Ballistic Pendulum 321

List of Figures

2.0 Literature Review on Tube Crushing 7

Figure 2.1: Typical example of the Euler buckling mode and resultant axial load-displacement curve of a thin-walled square tube [43] 9
Figure 2.2: Typical example of the progressive buckling mode and resultant axial load-displacement curve of a thin-walled square tube [43] 10
Figure 2.3: Typical examples of progressive buckling mode [44] 11
Figure 2.4: Progressive buckling in thin-walled cylindrical tubes 12
Figure 2.5: Progressive buckling in thin-walled square tubes 13
Figure 2.6: Dynamic plastic buckling 14
Figure 2.7: Classification chart for collapse modes of thin-walled aluminium alloy cylindrical tubes subjected to static axial loads [25] 15
Figure 2.8: Classification chart for collapse modes of thin-walled mild steel square tubes subjected to static axial loads[30] 16
Figure 2.9 : Deformation maps for square tubes subjected to (a) quasi-static (b) dynamic axial loading [45] 17
Figure 2.10 : Deformation maps for cylindrical tubes subjected to (a) quasi-static (b) dynamic axial loading [45] 17
Figure 2.11 : Deformed shaped of extruded aluminium rectangular tube[52] 20
Figure 2.12 : Deformed shape of the 52.6mm diameter steel tube in (a) annealed; and (b) as-received state [53] 21
Figure 2.13 : Symmetric deformation of dynamically loaded pre-dented square specimens 25
Figure 2.14 : Optimum dent depth for mild steel square tubes of width 50mm and wall thickness 1.2mm [30] 26
Figure 2.15 : The effect of opposing parallel indentations and opposing dished indentations on the ultimate buckling load [34] 27
Figure 2.16 : Quasi-statically crushed square tubes with opposing parallel cylindrical indentations [34] 27
Figure 2.17 : The effect of the depth of the corner dent on the Ultimate Buckling Load [33] 28

Figure 2.18 : Quasi-statically collapsed square tubes with opposing dished indentations [34] 29
Figure 2.19 : Shape of (a) full-dent and (b) half-dent introduced into the aluminium tube specimen [35]. 29
Figure 2.20 : Deformed aluminium tubes with schematic of the locations of triggering dent [35]. 30
Figure 2.21 : Symmetric axial crush response mode—ductile metallic alloy: axial crush specimen and un-deformed tube [58]. 30
Figure 2.22 : A typical load-displacement characteristics of aluminium alloy corrugated tubes [66] 33
Figure 2.23 : Quasi-Statically crushed square tubes with two opposing holes [34] 35
Figure 2.24 : The effect of the depth of dished indentations on ultimate buckling load of specimens with opposing combined imperfections [34] 37
Figure 2.25 : The effect of the diameter of the holes on ultimate buckling load of specimens with opposing combined imperfections [34] 37
Figure 2.26 : The effect of the depth of dished indentations on ultimate buckling load of specimens with opposing combined imperfections [34] 38
Figure 2.27 : Collapse profiles and load – deformation history of a spot-welded top-hat sections after impact testing at 10m/s[79] 39
Figure 2.28 : Test foam filled specimen geometry & typical material behaviour [82] 40
Figure 2.29 : Deformation behaviour of square and circular extrusions as a function of foam filler density [95, 96] 42
Figure 2.30 : Empty, monotubal filled and bitubal square crushed specimens[102] 43
Figure 2.31 : Square, hexagonal and octagonal monotubal crushed specimens[102] 44
Figure 2.32 : Photographs of sectional front and back views of crushed PVC tubes filled with mixed wood sawdust [105] 45
Figure 2.33 : Typical collapse modes of bare brittle metal and plastic metal tube [120] 47
Figure 2.34 : Failed hybrid tubes obtained from the axial crushing test [123] 48
Figure 2.35 : Axially crushed square tube (symmetric crushing mode) 50
Figure 2.36 : Basic collapse elements. (a) Type I (b) Type II[27]. 50

Figure 2.37 : Comparison between the predicted buckling shapes for material models with and without temperature effects. 63
Figure 2.38 : Dynamic buckling phenomena [144] 65
Figure 2.39: Variation of the stress wave speeds; depending on the stress state[136] 66
Figure 2.40: Numerical simulation of the influence of striking mass on final buckling shapes[137] 67
Figure 2.41: Numerical simulation of the influence of impact velocity on final buckling shapes[137] 68
Figure 2.42: Buckling shapes resulting from axial explosive loads; numerical predictions and test[141] 69
Figure 2.43 : Examples of multi-cell tubular structures[42] 74
Figure 2.44 : Tube layout investigated by Theobald and Nurick[160]. 75
Figure 2.45 : Static and dynamic compression tests of double chamber extrusions (centre) compared with simulations with and without failure criteria (left and right respectively) [161] 76

3.0 Literature Review on Blast Loading 79

Figure 3.1 : Typical record of Pressure-Time history of blast loads [190] 80
Figure 3.2 : Idealisation of the pressure-time history [194] 81
Figure 3.3 : Simplified pressure-time loading histories for typical blast wave[196] 82
Figure 3.4 : Illustration of charge stand-off distance and loading condition [198] 83
Figure 3.5 : Schematics of blast loading conditions 84
Figure 3.6 : Pressure load approximation by Bimha[200]. 86
Figure 3.7 : Expansion of explosive and its interaction with the plate for a load diameter 25mm and impulse 7.7Ns [202]. 88
Figure 3.8 : Failure associated with clamped meral beams loaded impulsively. 90
Figure 3.9 : Changing mid-point deflection for increasing Impulse 91
Figure 3.10 : Changing mid-point deflection for increasing Impulse 92
Figure 3.11 : Schematic drawing of different stiffener configuration 94
Figure 3.12 : Large inelastic deformation for localised blast loaded plate 95
Figure 3.13 : Cross sectional view of plate deformation for 1.6mm thick plates 96

Figure 3.14 : Photographs of typical Mode II response on front face and mode I response on back face 97
Figure 3.15 : Circular test plate with different boundary fixations 98
Figure 3.16 : Difference in plate deformation curvature near the boundary for built-in and test plates 98
Figure 3.17 : Schematic of different clamped boundary conditions 99
Figure 3.18 : Plastic hinge line pattern in a fully clamped rectangular plate subjected to a uniformly distributed impulsive velocity 101
Figure 3.19 : Maximum permanent transverse displacement for fully clamped rectangular plates subjected to uniformly distributed impulsive velocity[44] 102
Figure 3.20 : First yield results vs impulse for a 3x4mm single stiffened square plate[170] 105
Figure 3.21 : Plate mid-point displacement response [167]. 106
Figure 3.22 : Centre line profiles of a square plates at impulse 15Ns [167]. 106
Figure 3.23 : Predicted centreline failure profiles [167] 107
Figure 3.24 : Strain distribution at Mode II failure[167]. 107
Figure 3.25 : Severe element elongation predicting tearing[185] 109
Figure 3.26 : Formation of shear band at 45° and 135° predicting tearing[185] 109
Figure 3.27 : Comparison of predicted Mode II response of a double stiffened square plate with stiffener size 3x7mm undergoing at impulse 43Ns [178] 110
Figure 3.28 : Numerical simulation of sequence of deformation of experimental results for a localised blast impulse of 17.64Ns[204] 111

4.0 Experimental Details 113

Figure 4.1 : Tensile test specimen extraction from the mild steel extrusion. 115
Figure 4.2 : Quasi-static engineering stress-strain curve for tensile test cut out of the 50mm square tube (test speed 2mm/min) 115
Figure 4.3 : Quasi-static engineering stress-strain curve for tensile test cut out of the 75mm square tube 116
Figure 4.4 : Photo of the ballistic pendulum 117
Figure 4.5 : Schematic of the ballistic pendulum 118
Figure 4.6 : Square tube and blast load configuration 119
Figure 4.7 : Schematic of the quasi-static test set-up 120

Figure 4.8 : Photograph of the drop tester 121
Figure 4.9 : Photograph of dynamic axial crush set-up 122
Figure 4.10 : Schematic of dynamic axial crush set-up 122
Figure 4.11 : Schematic showing the experimental set-up for combined loading 124

5.0 Experimental Results 125

Figure 5.1 : Photograph showing typical response of 50mm square tube to localised blast load 126
Figure 5.2 : Photograph showing typical response of 75mm square tube to localised blast load 126
Figure 5.3: Photograph showing response of 50mm square tubes to localised blast load of 17mm load diameter 127
Figure 5.4 : Photograph showing deformed 50mm square tubes showing capping 127
Figure 5.5 : Photograph showing esponse of 50mm square tubes to localised blast load of 25mm load diameter 128
Figure 5.6 : Photograph showing cross-section view showing rebounded domes 128
Figure 5.7 : Photograph showing response of 75mm square tubes to localised blast load of 25mm load diameter 129
Figure 5.8 : Photograph showing deformed 75mm square tubes indicating thinning 129
Figure 5.9 : Photograph showing response of 75mm square tubes to localised blast load of 37.5mm load diameter 130
Figure 5.10 : Phtograph showing deformed 75mm square tubes showing partial tearing as a result of rebounded domes 130
Figure 5.11: Photograph showing typical response of rectangular plate subjected to localised blast load [223] 131
Figure 5.12 : Photograph showing tearing of the side of a rectangular plate subjected to localised blast load [223] 131
Figure 5.13 : Photograph showing the different modes of imperfections 133
Figure 5.14 : Photograph showing the transient response of quasi-statically crushed as received square tube 135

Figure 5.15 : Typical axial force-displacement graph for quasi-statically crushed as received square tube 135
Figure 5.16 : Photograph showing the transient response of quasi statically crushed square tube with circular cut-outs 136
Figure 5.17 : Typical axial force-displacement graph for quasi-statically crushed square tube with circular cut-outs 136
Figure 5.18 : Photograph showing the transient response of quasi-statically crushed square tube with simple mode I imperfections (load diameter 17mm) 138
Figure 5.19 : Typical axial force-displacement graph for quasi-statically crushed of square tubes with simple mode I imperfections (load diameter 17mm) 138
Figure 5.20 : Formation of dome shape under quasi-static axial load 139
Figure 5.21 : Photograph showing the transient response of quasi-statically crushed square tube with rebound domes imperfections 140
Figure 5.22 : Typical axial force-displacement graph for crushed square tube with rebound domes imperfections 140
Figure 5.23 : Photograph showing the transient response of quasi-statically crushed square tube with capping imperfections – (Load diameter 17mm) 142
Figure 5.24 : Typical axial force-displacement graph of quasi-statically crushed square tube with capping imperfections - (Load diameter 17mm) 142
Figure 5.25 : Photograph showing capping of square tube with 4.5g of explosive – load diameter 25mm 143
Figure 5.26 : Photograph showing the transient response of quasi-statically crushed square tube with capping imperfections – Load diameter 25mm 144
Figure 5.27 : Typical axial force-displacement graph of quasi-statically crushed square tube with capping imperfections - (Load diameter 25mm) 144
Figure 5.28 : Photographs showing Euler buckling post progressive collapse due to skew lobe formation 145
Figure 5.29 : Photograph showing dynamic axially crushed 50mm square tubes from different drop heights with drop mass of 210kg 147
Figure 5.30 : Photograph showing dynamic axially crushed 50mm square tubes from different drop heights with drop mass of 265kg 147
Figure 5.31 : Photograph showing dynamic axially crushed 50mm square tubes from different drop heights with drop mass of 329kg 148

Figure 5.32 : Photograph showing dynamic axially crushed 75mm square tubes from different drop heights with drop mass of 329kg 149
Figure 5.33 : Photographs showing dynamic axially crushed 50mm square tubes without and with hole cut-outs from a 3.26m drop height with drop mass of 329kg 150
Figure 5.34 : Photographs showing dynamic axially crushed 50mm square tubes without and with hole cut-outs from a 3.5m drop height with drop mass of 329kg 151
Figure 5.35 : Photographs showing dynamic axially crushed 50mm square tubes with hole cut-outs 12.5mm in diameter by drop mass of 329kg 151
Figure 5.36 : Photographs showing dynamic axially crushed 50mm square tubes from a 3m drop height with drop mass of 329kg 152
Figure 5.37 : Photographs showing dynamic axially crushed 75mm square tubes from 3m and 3.5m drop heights with drop mass of 329kg 153
Figure 5.38 : Photographs showing dynamic axially crushed 50mm square "perfect" and "blast loaded" tubes with drop mass of 210kg 155
Figure 5.39 : Photographs showing dynamic axial crushed 75mm square tubes without and with blast imperfection 156
Figure 5.40 : Photographs showing dynamic axially crushed blasted loaded 50mm tube with drop mass of 210kg from 4m drop height 157
Figure 5.41 : Photographs showing dynamic axial crushed 50mm square tubes with blast imperfection caused by 4.5g of PE4 at load diameter 17mm 158
Figure 5.42 : Photographs showing dynamic axially crushed blasted loaded 50mm tube with drop mass of 210kg from 4m drop height 159
Figure 5.43 : Photographs showing dynamic axial crushed 50mm square tubes with blast imperfection caused by 4.75g of PE4 at load diameter 17mm 160
Figure 5.44 : Photographs showing dynamic axial crushed 75mm blast "capped" square tubes 161
Figure 5.45 : Photographs showing dynamic axial crushed 50mm square tubes with and without imperfections caused by explosive of load diameter of 17mm with drop mass of 329kg from a nominal height of 3.26m 162
Figure 5.46 : Photographs showing dynamic axial crushed 75mm square tubes without and with blast imperfection 164
Figure 5.47 : Photograph showing unstable buckling of 50mm square tube 164

6.0 Analysis of Experimental Results 165

Figure 6.1 : Graph of impulse versus mass of explosive 167
Figure 6.2 : Graph of impulse vs mass of explosive for ME ranging from 1 to 6g 168
Figure 6.3 : Graph of maximum deflection v/s impulse 169
Figure 6.4 : Photograph showing geometrically "perfect" square tubes crushed quasi-statically in the axial direction (increasing cross-head speed from left to right) 170
Figure 6.5 : Photograph showing square tubes with and without imperfections crushed quasi-statically 175
Figure 6.6 : Axial force vs displacement curve for tubes with and without dome imperfections crushed quasi-statically 176
Figure 6.7 : Axial force vs displacement curve for "perfect" and holed tubes crushed quasi-statically 177
Figure 6.8 : Mean crush load of geometrically "perfect" and "imperfect" tubes crushed quasi-statically 178
Figure 6.9 : Ultimate peak load of geometrically "perfect" and "imperfect" tubes crushed quasi-statically 179
Figure 6.10 : Load efficiency of geometrically "perfect" and "imperfect" tubes crushed quasi-statically 180
Figure 6.11 : Photograph showing comparison between quasi-statically crushed tubes with rebound imperfections with and without heat treatment 181
Figure 6.12 : Axial force vs displacement curve for tubes with rebound imperfections crushed quasi-statically 181
Figure 6.13 : Photograph showing tubes collapsing in unstable mode 182
Figure 6.14 : Graph comparing predicted crushed distance with experiments 191
Figure 6.15 : Graph showing calculated mean crushed force against measured crushed distance for "perfect" square tubes 192
Figure 6.16 : Graph showing calculated mean crushed force against measured crushed distance for square tubes with blast induced imperfections 193
Figure 6.17 : Geometric efficiency of geometrically "perfect" and "imperfect" tubes crushed dynamically 194

Figure 6.18 : Photographs showing dynamic axially crushed 50mm square tubes exposed to 2g of explosive, from 5m drop height with drop mass of 210kg (opposite sides touching in highlight) 195
Figure 6.19 : Photographs showing dynamic axially crushed 50mm square tubes, exposed to explosive load of 17mm in diameter, from 4m drop height with drop mass of 210kg 196
Figure 6.20 : Photograph showing dynamic axially crushed 50mm square tubes, exposed to explosive load of 17mm in diameter, from 3.26m drop height with drop mass of 329kg 197
Figure 6.21 : Photograph showing comparison between quasi-statically and dynamically crushed tubes 198

7.0 Finite Element Formulation 199

Figure 7.1 : A schematic of a C3D8R element, showing node numbering and co-ordinate system 201
Figure 7.2 : A schematic of a S4R element, showing node numbering and co-ordinate system 202
Figure 7.3: ½ tube FE Model of tube showing assigned element types 204
Figure 7.4 : Graph of true stress vs logarithmic strain 207
Figure 7.5 : A comparison of the normalised Young's Modulus and yield stress 210
Figure 7.6 : ½ tube FE Model showing applied boundary conditions 212
Figure 7.7 : Explosive disc 214
Figure 7.8 : Pressure distribution with respect to time 214
Figure 7.9 : Axi-symmetric schematic of the localised blast of PE4 explosive, using AUTODYN 2D 215
Figure 7.10 : Plot of pressure – time history of discrete points along the plate radius 216
Figure 7.11 : Plot of the normalised maximum pressure envelop; Note explosive disk radius is 8.5mm 216
Figure 7.12 : ½ tube FE Model showing dynamic axial loading condition 219
Figure 7.13 : ½ tube FE Model showing combined loading condition 220

8.0 Finite Element Simulation Results 221

Figure 8.1 : Displacement history at various points along the tube profile 222
Figure 8.2 : Monitored points along 50mm tube profile 222
Figure 8.3 : Prediction of Mode I response of a 50mm square tube (Impulse : 5.7Ns, Load diameter : 17mm, Mass of explosive : 3.5g) 224
Figure 8.4 : Prediction of Mode I response of a 50mm square tube (Impulse : 5.5Ns, Load diameter : 25mm, Mass of explosive : 3g) 225
Figure 8.5 : Prediction of Mode I response of a 75mm square tube (Mass of explosive : 4g) 227
Figure 8.6 : Prediction of Mode I "rebound" response of a 50mm square tube (Impulse : 7Ns, Load diameter : 25mm, Mass of explosive : 3.5g) 228
Figure 8.7 : Comparison of experimental and numerical predictions of Mode I deformation 229
Figure 8.8 : Prediction of Mode IIc response of a 50mm square tube (Impulse : 8.6Ns, Load diameter : 17mm, Mass of explosive : 4.5g) 232
Figure 8.9 : Prediction of Mode I "rebound" response of a 75mm square tube 233
Figure 8.10 : Prediction of Mode IIc response of a 75mm square tube 234
Figure 8.11 : Prediction of blast response of 75mm square tube 235
Figure 8.12 : Predicted crush response of a 50mm square tube to a 329kg mass axially dropped from a height of 3m (Impact velocity 7.76m/s) 237
Figure 8.13 : Predicted crush response of a 75mm square tube to a 329kg mass axially dropped from a height of 3.8m (Impact velocity 8.67m/s) 238
Figure 8.14 : Predicted crush responses of 50mm square tubes with and without circular cut-outs to 329kg mass impacted at 8m/s (hole diameter increasing from left to right) 240
Figure 8.15 : Predicted axial force-displacement graph for dynamically crushed tube with and without circular cut-outs using Material M 242
Figure 8.16 : Predicted axial force-displacement graph for dynamically crushed tube with and without circular cut-outs using Material T 242
Figure 8.17 : Predicted collapse mode of a 50mm square tube with simple Mode I imperfections created by two 25mm blast loads 244

Figure 8.18 : Predicted axial force-displacement graph for dynamically crushed 50mm square tube with simple Mode I imperfections created by two 25mm blast loads 245
Figure 8.19 : Collapse sequences of a 50mm square tube with simple Mode I imperfections created by two 25mm blast loads 246
Figure 8.20 : Contour plots of a crushed 50mm square tube with induced simple Mode I imperfections created by two 25mm blast loads 247
Figure 8.21 : Predicted collapse mode of 75mm square tube with induced simple Mode I imperfections created by two 37.5mm blast loads 248
Figure 8.22 : Predicted axial force-displacement graph for dynamically crushed 75mm tube with induced simple Mode I imperfections created by two 37.5mm blast loads 249
Figure 8.23 : Collapse sequences of a 75mm square tube with induced simple Mode I imperfections created by two 37.5mm blast loads 250
Figure 8.24 : Contour plots of a crushed 75mm square tube with induced simple Mode I imperfections created by two 37.5mm blast loads 251
Figure 8.25 : Comparison of predicted collapse mode of a 50mm square tube with induced rebound imperfections created by two 17mm blast loads 252
Figure 8.26 : Predicted axial force-displacement graph for dynamically crushed tube with induced rebound imperfections created by two 17mm blast loads 253
Figure 8.27 : Collapse sequences of a 50mm square tube with induced rebound imperfections created by two 17mm blast loads 254
Figure 8.28 : Contour plots of a crushed 50mm square tube with induced rebound imperfections created by two 17mm blast loads 255
Figure 8.29 : Comparison of predicted collapse mode of a 50mm square tube with rebound induced imperfections created by two 25mm blast loads 256
Figure 8.30 : Final collapse mode of a 50mm square tube with rebound induced imperfections created by two 25mm blast loads 257
Figure 8.31 : Comparison of predicted collapse mode of a 50mm square tube with induced capping imperfections created by two 17mm blast loads 259
Figure 8.32 : Collapse sequences of a 50mm square tube with induced capping imperfections created by two 17mm blast loads 260
Figure 8.33 : Contour plots of a crushed 50mm square tube with induced capping imperfections created by two 17mm blast loads 262

Figure 8.34 : Comparison of experimental and numerical predictions of crushed distance 263

9.0 Discussion of Finite Element Results 265

Figure 9.1 : Crushed 50mm tubes with asymmetric blast response 266
Figure 9.2 : Rectangular pressure distribution with respect to time (loading definition for blast load 2) 267
Figure 9.3 : ½ tube FE Model showing different loading conditions 267
Figure 9.4 : Predicted collapse mode of a 50mm square tube with blast-induced asymmetric imperfections 269
Figure 9.5 : Collapse sequences of a 50mm square tube with blast-induced asymmetric imperfections 270
Figure 9.6 : Comparison of predicted collapse mode of 50mm square tubes with the same induced blast imperfections to impact velocity of 8m/s with different drop masses 271
Figure 9.7 : Predicted axial force-displacement graph for dynamically crushed tube with same induced blast imperfections to impact velocity of 8m/s with different drop masses 272
Figure 9.8 : Comparison of predicted collapse mode of 50mm square tubes with the same induced blast imperfections to 165kg drop mass impacted at different velocity 273
Figure 9.9 : Predicted axial force-displacement graph for dynamically crushed tube with same induced blast imperfections to 329kg at different impact velocities 274
Figure 9.10 : Comparison of predicted collapse mode of 50mm square tubes with the same induced blast imperfections and initial impact energy of 10.5kJ 275
Figure 9.11 : Predicted axial force-displacement graph for dynamically crushed tube with same induced blast imperfections and initial impact energy of 10.5kJ 276
Figure 9.12 : Comparison of predicted collapse mode of 50mm square tubes with circular cut-outs of different diameters 277
Figure 9.13 : Graph of axial force vs cut-out diameter showing the effect on ultimate peak load and mean crush force 278

Figure 9.14 : Predicted geometric and load efficiencies of 50mm square tubes with circular cut-outs 279
Figure 9.15 : Stress state prior to applying the dynamic axial load 280
Figure 9.16 : Predicted deformed shapes for 50mm square tube with imperfections created by 25mm blast loads with different stress state before dynamic loading 281
Figure 9.17 : Predicted axial force-displacement graph for dynamically crushed 50mm tube with different stress state prior to dynamic loading 282
Figure 9.18 : Predicted blast-induced imperfections for 50mm tube at various impulses 283
Figure 9.19 : Predicted deformation profile along central longitudinal axis of 50mm tube at various impulses 284
Figure 9.20 : Predicted buckling shapes for dynamic axially loaded 50mm tubes with imperfections induced by different blast loads 285
Figure 9.21 : Predicted axial force-displacement curves for some dynamic axial load of 50mm square tubes with imperfections induced by different blast loads 287
Figure 9.22 : Predicted blast-induced imperfections for 75mm tube at various impulses 288
Figure 9.23 : Predicted deformation profile along central longitudinal axis of 75mm tube at various impulses 289
Figure 9.24 : Predicted buckling shapes for dynamic axially loaded 75mm tubes with imperfections induced by different blast loads 290
Figure 9.25 : Predicted axial force-displacement curves for some dynamic axial load of 50mm square tubes with imperfections induced by different blast loads 292
Figure 9.26 : Comparisons of transient crush behaviour of different size tubes with different blast-induced imperfections 295

List of Tables

4.0 Experimental Details 113

Table 4.1 : Plate material properties and geometry 116
Table 4.2 : Ballistic pendulum details 118

6.0 Analysis of Experimental Results 165

Table 6.1 : Blast test results for 50mm square tubes 165
Table 6.2 : Blast test results for 75mm square tubes 166
Table 6.3 : Quasi-static crush test results for as received square tubes 170
Table 6.4 : Mean static crushing load for 50mm square tubes 171
Table 6.5 : Ultimate buckling load for 50mm square tubes 172
Table 6.6 : Quasi-static crush test results for induced geometric imperfection square tubes 173
Table 6.7 : Dynamic crush test results for as received square tubes 183
Table 6.8 : Dynamic crush test results for square tubes with circular cut-outs imperfections 186
Table 6.9 : Dynamic crush test results for tubes with simple Mode I imperfections 187
Table 6.10 : Dynamic crush test results for tubes with rebound imperfections 188
Table 6.11 : Dynamic crush test results for tubes induced cap imperfections 189
Table 6.12 : Influence of load diameter on contact area 195

7.0 Finite Element Formulation 199

Table 7.1 : Material properties of test plate 211
Table 7.2 : Typical values of r_5, r_p and k obtained for different load diameters. 217

8.0 Finite Element Simulation Results 221

Table 8.1 : Modes of failure for plates subjected to blast load 230
Table 8.2 : Summary of predicted results for dynamic axial load of square tube with and without circular cut-outs 241

9.0 Discussion of Finite Element Results 265

Table 9.1 : Summary of predicted results for dynamic axial load of square tube with same induced blast imperfections to impact velocity of 8m/s with different drop masses 272
Table 9.2 : Summary of predicted results for dynamic axial load of square tube with same induced blast imperfections to 329kg at different impact velocities 274
Table 9.3 : Summary of predicted results for dynamic axial load of square tube with same induced blast imperfections and initial impact energy of 10.5kJ 275
Table 9.4 : Summary of predicted results for dynamic axial load of 50mm square tube with and without circular cut-outs 278
Table 9.5 : Summary of predicted results for dynamic axial load of 50mm square tube with different stress state prior to dynamic loading 281
Table 9.6 : Predicted maximum deflection of blast-induced imperfections for 50mm tube at various impulses 283
Table 9.7 : Summary of predicted results for dynamic axial load of 50mm square tubes with imperfections induced by different blast loads 286
Table 9.8 : Predicted maximum deflection of blast-induced imperfections for 75mm tube at various impulses 288
Table 9.9 : Summary of predicted results for dynamic axial load of 75mm square tubes with imperfections induced by different blast loads 291

Nomenclature

Upper Case

A	Cross sectional area of tube
A_j	Material parameters measured at or below $\theta_{transition}$
B	Plate breadth
C	Tube width
D	Cut-out diameter
D_t	Tube Diameter (=2R)
E	Young's modulus
E_1	Internal energy for type I basic folding element
E_2	Internal energy for type II basic folding element
$E_{absorbed}$	Total energy absorbed
F	Axial force
G	Striking mass
H	Thickness (plate and tube)
I	Impulse applied to the structure
L	Length of tube; Length of plate
L_B	Half beam length
M	Total mass of pendulum
ME	Mass of explosive
M_o	Fully plastic bending moment
P	Pressure
P_m	Mean static crushing load
$\bar{P}_m$	Average mean static crushing load
P'_m	Mean dynamic crushing load
P_{MAX}	Maximum crushing load
P_o	Peak Pressure
P_{ult}	Ultimate buckling load
R	Tube radius
R_o	Load radius
S	Material parameters measured at or below $\theta_{transition}$
S_e	Specific energy
T	Time period of pendulum
V_b	Burn speed of the explosive
V_o	Initial impulsive velocity

W_f	Maximum permanent transverse displacement
W	Width of plate
Z	Length of pen

Lower Case

a	Characteristic cut-out dimension
b	Radius of toroidal shell element
b_e	Von Karmar effective width
b_f	Final radius of toroidal shell element
c	Specific heat
e_G	Geometric efficiency
e_L	Load efficiency
e_E	Energy efficiency
d	Load diameter ($2 \times R_o$)
k	Decay constant
l	Half initial distance between plastic hinges
m	Mass of specimen
n	Strain rate enhancement
p	Material parameters measured at or below $\theta_{transition}$
q	Material parameters measured at or below $\theta_{transition}$
r	Radial distance for explosive centre
r_b	Burn radius
r_p	Radial distance at which pressure = 0
t	time
t_{blast}	Duration of blast
u	Displacement
$\dot{u}$	Velocity
$\ddot{u}$	Acceleration
v	Impact velocity of striking mass
v_m	Mean impact velocity
v_o	Striking velocity

Greek Characters

β	Aspect ratio (B/D)
β_c	Damping constant
δ	Mid-point deflection
δ_a	Effective crushing distance for asymmetry and extensional mode
δ_t	Tube crushing distance
δ_1	Effective crushing distance for symmetry collapse mode
ε_{eq}	Current value of the logarithmic strain
ε_N	Strain at necking initiation
ε_{nom}	Nominal strain
$\bar{\varepsilon}^{pl}$	Equivalent plastic strain
ε_{ln}^{pl}	logarithmic plastic strain
$\Delta\bar{\varepsilon}^{pl}$	Increment of the equivalent plastic strain
$\bar{\varepsilon}_f^{pl}$	Strain at failure
$\dot{\varepsilon}$	Strain rate
$\dot{\varepsilon}_o$	Material constant
θ	Current temperature
$\hat{\theta}$	Non-dimensional temperature
θ_{melt}	Melting temperature
$\theta_{transition}$	Transition temperature
ϕ	Hole cut-out diameter
ϕ_q	Dimensionless impulse for plates (Damage number)
ϕ_{q_j}	Modified dimensionless impulse for plates (Damage number)
ϕ_t	Dimensionless impulse for tubes (Damage number)
λ	Jones dimensionless impulsive velocity
ξ_o	Geometry parameter
ζ_{o_j}	Blast loading parameter
Γ	Loading parameter
η	Material constant
μ	Mass per unit length
ν	Poisson's ratio
ρ	Material density

σ	Axial stress
σ_y	Material static yield stress
σ_o	Plastic flow stress
σ_{true}	True stress
σ'_y	Dynamic yield stress
σ_{nom}	Nominal stress
σ_θ	Static yield stress at the reference temperature of the tensile test

Acknowledgement

The author is indebted to many departmental staff who generously provided their valued advice and guidance throughout the course of this dissertation. In particular, the author acknowledges the contributions of technical staff of the Department of Mechanical Engineering, in particular Mr L. Watkins, Mr W. Slaverse, Mr D. Jacobs Mr H. Tomlinson, Mr P. Jacobs and Mr G. Newins who help building the drop tester and prepare the test specimens, Mrs P. Park-Ross from the Centre of Material Science for her assistance in characterising the specimen material, Mr. K. Balchin for his priceless effort in designing the drop tester and making it safe and the invaluable assistance received from Mr V. H. Balden, for his expert advice in the development of the Finite Element models. Thanks also go to Mr P. Smith from the Department of Mechanical Engineering, Impact Research Centre, University of Liverpool for his help with the drop test experiments.

The author also wishes to thank all the group members of the Blast Impact and Survivability Research Unit; (BISRU) for their friendship and assistance. Special mention goes to Dr G. Langdon and Mr N. Jacob for their selfless and prompt help.

The author's thanks also go to the Blast Impact and Survivability Research Unit; (BISRU), the Department of Mechanical Engineering, Armaments Corporation of South Africa; (ARMSCOR) and the National Research Foundation of South Africa; (NRF) for their financial support and to the Department of Mathematics for providing the extra financial support in the form of tutorship.

Special thanks go to Prof. G. N. Nurick, the author's supervisor for his continued and precious support and guidance. And finally but not least, the author is grateful to his parents; Georges and Bernadette, siblings; Belinda, Belaine and Clive and friends; Connie Lie, Natalie Too, Beverly Bailey, Dawn Beckett, Chris Warner, Maria Tito and Rajive Rogbeer for their never-ending encouragements.

1.0 Introduction

The potential for accidents is always on the rise with the ever-increasing demand for mass transport whether by land, air or sea. The life changing injuries and damage to property resulting from these accidents present huge financial and emotional burden on society. According to Road Traffic Management Corporation[1], each day in the year 2003-2004, on average 36 lives were lost, 20 people became permanently disabled and around 100 people were seriously injured on South African roads. The 2004 World Health Organization report[2] on road traffic injury prevention states that approximately 1.2million people are killed and 50million people are injured in road traffic accidents each year. Scientists and engineers face the escalating challenge of finding solutions to greatly improve the ability of vehicles to both prevent and reduce occupant injuries in the event of accidents.

Significant reductions in injuries and damage can be achieved through the development of better transportation structures. Lu and Yu[3] define the term *crashworthiness* as "the quality response of a vehicle when it is involved in or undergoes an impact". For a better crashworthiness performance, the vehicle must experience less damage and protect its occupants and contents by maintaining structural integrity and absorbing the large amount of kinetic energy in a controllable and predictable manner or at a predetermined rate. In vehicles, components such as air bags, seat belts, crumple zones, side impact protection, interior padding and head rests are crashworthiness features. These features may or may not be present in a particular vehicle and may or may not work even if present. According to Technical Services Forensic Engineering[4], all of these items have been available since the early 1970's and many are still not found as standard features in some current production vehicles.

Thin-walled extruded tubes in various shapes and sizes, however, have been widely used for their energy absorption capabilities in the crashworthiness design of vehicles (cars, buses, trains, and aeroplanes) where the life of passengers is at risk in the event of a collision. In general, the extruded tubes can sustain high impact loads with large geometric deformations, strain hardening effects, strain-rate effects, temperature effects, and various interactions between different deformation modes such as bending and stretching. These structures convert the input kinetic energy into strain energy by plastic deformation.

There have been numerous studies carried out in the area over the last few decades, for example Pugsley and Macaulay[5], Alexander[6], Abramowicz and Jones [7-9]. Under axial loading conditions, thin-walled tubular structures exhibit an initial peak force which is much greater than the subsequent peak force. In crashworthiness situations, this initial peak force is highly undesirable. The idea of using initiators to start the collapse process of these structures at a specific location with a reduced initial peak force (ideal in crashworthiness situations) has been previously explored, for instance Thornton and Maggee[10]. These initiators also referred to as imperfections, can be either material or/and geometric modifications to the structure. Generally imperfections are thought of as slight deviation of the structural geometry due to the manufacturing process. However for the purpose of this thesis, imperfections are defined as any deviation from the as received condition of the tubes including hole cut outs and blast-induced initiators.

This thesis reports on the results of an experimental and numerical investigation into the dynamic axial response of extruded square tubes subjected to two localised blast loads before an impact load. The localised blast loads are used to induce both geometric and material changes to the tubular structure with a view to weaken the structure and locally change its material properties.

The square tubes used for this thesis are 50x50x1.5mm and 75x75x1.6mm. The blast load diameter to tube width ratio is kept constant at 0.33 and 0.5. The mass of the explosive is, however, varied to induce different geometric imperfections (non-touching domes, rebound domes and capping domes). Depending on the severity of the blast load, the material properties will be affected accordingly. The drop mass and drop height are also varied to produce different impact energies. The response of the square tube is described by its deformation resulting from the blast loads and its folding mechanisms as a result of the axial load.

The numerical analysis is divided into two parts. Firstly, an investigation using the hydro-dynamic code AutoDYN to model the explosive interaction with a plane structure. The results obtained from the AutoDYN simulations are then applied to the explicit dynamic finite element program; ABAQUS/*Explicit* v6.5-6 to simulate the large inelastic deformation and tearing mode of the square tube due to the blast loads. The buckling mode of the square tube due to the dynamic impact load is also modelled using ABAQUS/*Explicit* v6.5-6. The numerical predictions are compared with the experimental results.

The purpose of this investigation is to ascertain the influence of the blast loads on the energy absorption characteristics of the tube.

The objectives of this thesis are to:

(a) primarily, perform experiments to assess how two explosive charges on opposite sides of a square tube would affect the thin-wall structure and reduce its crush load (in particular the first peak and mean crush load) when compressed in the axial direction.

(b) perform numerical analysis to model the dynamic response of square tubes to two simultaneous localised blast loads followed by a dynamic axial load.

(c) use the numerical model with temperature dependent material properties to attempt to gain a better understanding of the blast load effects on the thin-walled structure and tube crushing mechanics.
(d) compare numerical model to experimental results.
(e) numerically investigate the influence of material property changes and geometry changes on the energy absorption characteristics of the square tube.
(f) draw conclusions and recommendations based on the findings.

This thesis report is based on information from experiments undertaken at the Blast Impact and Survivability Research Unit (BISRU), University of Cape Town and some drop tests conducted at the Impact Research Centre (IRC), University of Liverpool. The drop tests carried out at the IRC were done before the drop tester facility at BISRU was commissioned. While these drop tests are limited in drop mass (maximum 210kg) higher impact velocities can be achieved.

While it is extremely important to obtain material data through extensive material testing at different strain rates and temperatures using different available methods (hopkinson bar tests, tensile tests) the material data used for this report is limited to tensile testing at a quasi-static rate at room temperature.

The results obtained from the numerical simulations are compared with experiments by means of global deformed shape and measured crushed distance. The force-displacement data obtained from the numerical simulations are used to investigate the performance of the dynamically loaded tubes as instruments required to measure transient experimental data could not be purchased due to cost issues.

The results of an extensive literature review that covers the response of extruded tubes to axial loads and structures to blast loads and are reported in Chapters 2 and 3 respectively. The experimental procedures are briefly described in Chapter 4 with the experimental results and the physical indicators such as tube deformation, tearing and

failure modes given in Chapter 5. An analysis of the experimental results which includes graphs and comparisons with other work is given in Chapter 6. Chapter 7 sets out the methods of finite element solutions. This included the steps taken to achieve a final working model and the justification for the modelling decisions. The results obtained from the numerical model are presented and compared with experimental results in Chapter 8. A parametric study in the form of finite element simulations is discussed and analysed in Chapter 9. Conclusions are drawn and recommendations are made based on the findings in Chaptets 10 and 11 respectively.

2.0 Literature Review on Tube Crushing

Numerous investigations have been carried out on tubes, loaded either quasi-statically or dynamically in the axial direction and bending. The studies on axially impacted thin-walled sections having various cross-sections have been published over the years, for example circular, square, hexagonal and octagonal Refs[5-17]. There have also been studies on oblique loading of square aluminium tubes, for instance Børvik *et al.*[18] and Reyes *et al.*[19]. However, this chapter will only cover a literature survey on the crushing of tubes, dealing mostly with square tubes loaded axially.

An ideal crash would be no crash at all. But if one is going to crash one will want the best possible chances of survival and surviving a crash is all about kinetic energy. Tubular structural members can absorb large amounts of kinetic energy when deformed under compression in any impact situations. Pugsley and Macaulay[5] and Alexander[6] pioneered the studies on the behaviour of thin-walled structures for their absorbing kinetic energy capabilities. Since then, there has been continued interest on the axial crushing behaviour of thin-walled structures which were recently overviewed by Alghamdi[20] and Jones[21].

Extensive experimental and theoretical studies on the axial collapse of thin-walled tubes of circular, square or rectangular cross-sections under static or dynamic loading conditions have been carried out to characterise the mode of collapse, the ultimate peak force, the mean force and the energy absorption, Refs[5-9, 22-28]. With the demand for increased safety, the optimisation of the energy absorption characteristics of these thin-walled tubular structures has become the focus of studies for a number of years. Further studies, Refs[29-35] show that a core of such studies has been on the use of geometric imperfections in the tubes to decrease the ultimate buckling load and to induce preferred buckling modes.

The recorded responses of these structural elements have been compared with the responses predicted analytically and numerically. Reviews of the work conducted in this field have been published by many researchers, for example Refs[35-37]. Other studies to optimise the cross-section of these thin-walled structures to absorb kinetic energy effectively have also been numerically carried out, for instance Refs [38-42].

The literature review carried for this section is divided into three main sections:

- Experimental studies
- Theoretical analysis
- Computational predictions

2.1 Experimental studies

2.1.1 Modes of buckling

Thin-walled square and cylindrical tubes loaded axially may fail in a number of distinct collapse modes. These modes of collapse are influenced by the tube material, tube length, cross-sectional dimensions and wall thickness and, can be classified as:

i. Euler buckling
ii. Progressive buckling
iii. Dynamic plastic buckling

2.1.1.1 Euler buckling

In the Euler buckling mode, the tube bends in the same way as a strut under axial loading. As the tube begins to collapse, a plastic hinge mechanism develops at a point in the tube which causes the tube to buckle such that it folds over on itself. The longitudinal axes on either side of the hinge are thus no longer parallel. An example of Euler buckling is shown in Figure 2.1(a).

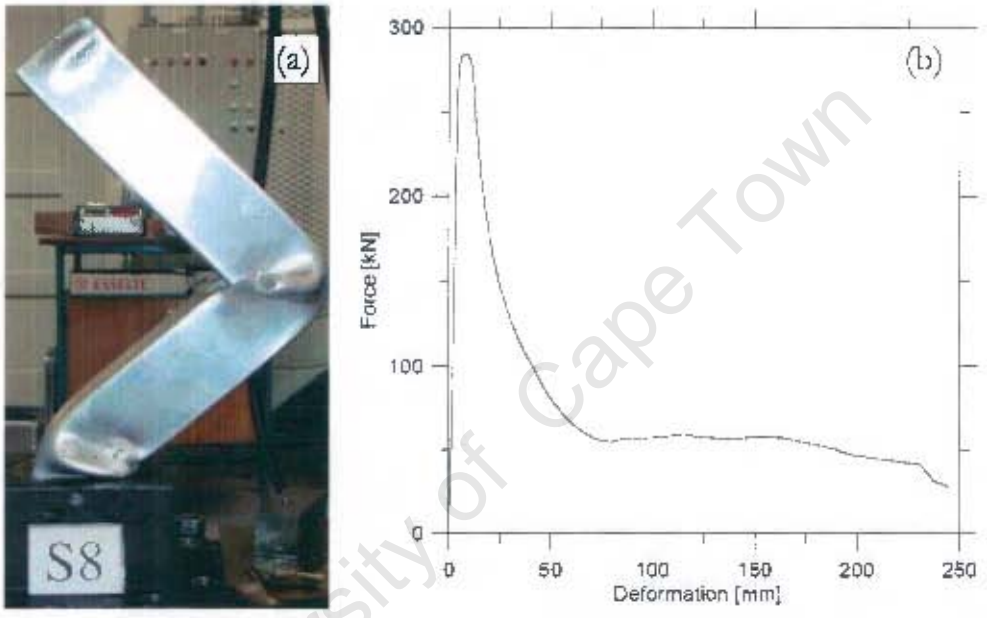

Figure 2.1: Typical example of the Euler buckling mode and resultant axial load-displacement curve of a thin-walled square tube [43]

A typical load-displacement curve of a square tube which has failed in the Euler buckling mode is shown in Figure 2.1(b). In this particular instance, the tube is made from aluminium and is 639mm long, 80mm wide and has a wall thickness of 4.5mm. These figures equate to a length-width ratio of 8 and thickness-width ratio of 0.06. The proportion of the tube material absorbing energy through plastic work is relatively small compared with the total tube length. The initial peak in the force–displacement curve is followed by a drop to a low and relatively constant force level. This low energy characteristic thus makes the Euler buckling mode a non-desirable mode for energy absorption.

2.1.1.2 *Progressive buckling*

When a thin-walled tubular structure is subjected to an axial compressive load which exceeds the yield strength of the material its load capacity decreases significantly. In the case of progressive buckling, the load carrying ability of the tube decreases to a minimum and then increases again and begins to oscillate about a mean buckling force thereafter. Figure 2.2 shows the load-deflection curve for the progressive buckling phenomenon of a thin-walled square tube which exhibits a repeated pattern after reaching the first peak. The first peak corresponds with the formation of plastic hinges in the structure. The walls of the tube fold around and extend at the hinges. One layer of folds occurs at a time and once the first layer is completely formed the next layer begins. The subsequent repeated peaks represent subsequent plastic hinges. Each pair of peaks in Figure 2.2 is associated with the development of a wrinkle or buckle shown in Figure 2.3. Usually the development of these wrinkles start at one end of the tube, then progresses sequentially along the length of the tube. The physical crumpling has been described extensively by Jones[44], amongst others.

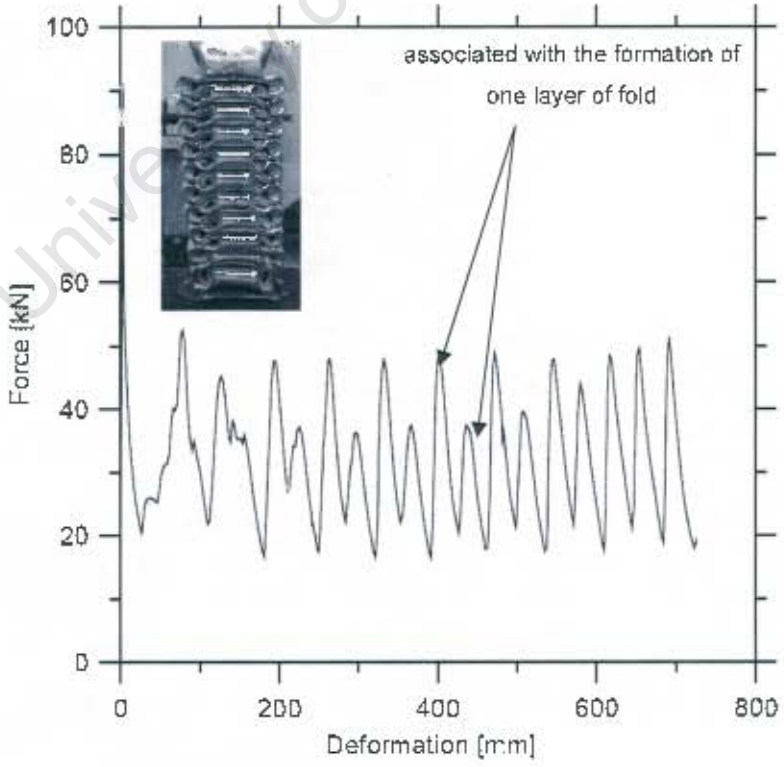

Figure 2.2: Typical example of the progressive buckling mode and resultant axial load-displacement curve of a thin-walled square tube [43]

Figure 2.3: Typical examples of progressive buckling mode [44]

Different modes of progressive buckling mode

When thin-walled cylindrical and square tubes buckle in the progressive buckling mode, they buckle forming a number of different lobe shapes or deformation modes. These different buckling modes all have the same oscillatory load displacement curves. However, their respective mean crushing loads differ from mode to mode. Nonetheless, this is an energy absorbing efficient mode of collapse because most of the tube material is utilised in energy absorption through plastic work.

Deformation modes in cylindrical tubes

Progressive buckling of thin-walled cylindrical tube results in either axi-symmetric (Concertina mode) or non-axi-symmetric (Diamond mode) modes of collapse[8] as shown in Figure 2.4.

i. *Concertina Mode*

In this mode, the plastic hinges form around the circumference of the tube at the top axi-symmetrically. The tube deforms to form sequential folding in ring shaped lobes along the length of the tube.

ii. *Diamond Mode*

In this failure mode, the tube buckles progressively by forming sequential folds accompanying a change in the cross-section shape of the tube. Diamond shaped sections around the circumference of the tube with different number of lobes are obtained.

Figure 2.4: Progressive buckling in thin-walled cylindrical tubes
On the left : Concertina Mode ; Centre and right : Diamond Mode[8]

Deformation modes in square tubes

Abramowicz and Jones[7] identified four distinct progressive buckling modes of failure for thin-walled square tubes, namely symmetric, asymmetric mixed collapse modes A and B, and an extensional collapse mode of failure. These modes of collapse are shown in Figure 2.5.

i. *Symmetric mode*

This mode describes three geometric folding mechanisms all with identical crushing loads and energy absorption characteristics. The first and subsequent individual lobes which develop possess similar characteristics.

a. Two opposite lobes move outwards while the remaining two lobes move inwards in one layer.
b. Three lobes move inwards and one outwards in one layer.
c. All four individual lobes in one layer move inwards

ii. *Asymmetric mixed collapse mode A*

In this mode of failure, the tube collapses with a combination of symmetric layers (as described above) and layers with three individual lobes deforming outwards and one inwards.

iii. *Asymmetric mixed collapse mode B*

In this mode of failure, the tube crushes with a combination of symmetric layers (as described above) and layers with two adjacent lobes deforming outwards with the other two adjacent lobes deforming inwards.

iv. *Extensional mode*

In this mode of collapse all four lobes deform outwards.

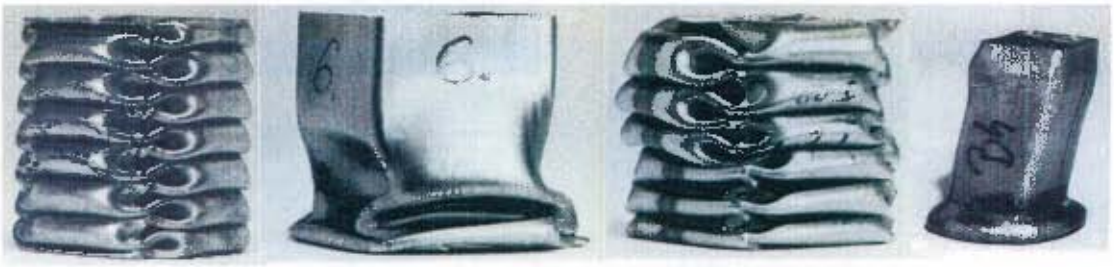

Figure 2.5: Progressive buckling in thin-walled square tubes
From left to right : symmetric, asymmetric mixed collapse modes A and B, extensional [7]

2.1.1.3 Dynamic plastic buckling

In the case of dynamic progressive buckling of thin-walled tubes subjected to axial loads, the impact loads are applied sufficiently slowly so that neither axial nor lateral inertia effects have a significant effect on the buckling process. The load duration is much longer than the transit time of an elastic stress wave which propagates along the tube. Consequently, the tube is unable to support a mean dynamic axial load greater than the static value when ignoring the influence of material stain rate sensitivity. As a result, the deformed profile of the tube is similar for both static buckling and dynamic progressive buckling.

If a thin-walled tube is subjected to a sufficiently severe dynamic axial load then structural inertia effects will produce the phenomenon of dynamic plastic buckling. In this case, the deformed shape of the tube as shown in Figure 2.6 may be quite different from the dynamic progressive buckling for an axially loaded thin-walled cylindrical tube. The tube is wrinkled over the entire length when buckled dynamically in contrast to the dynamic progressive case with wrinkling confined to one end.

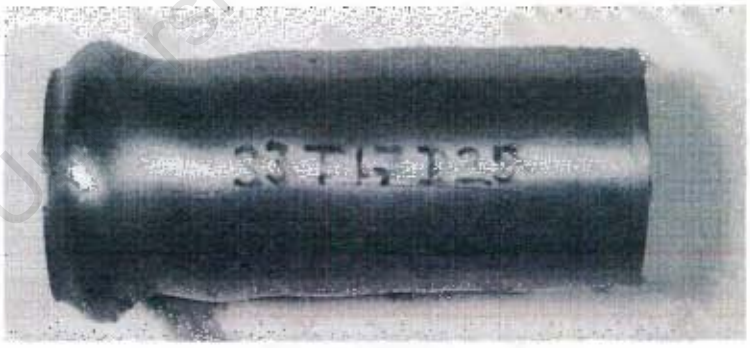

Figure 2.6: Dynamic plastic buckling.
Permanent profile of an aluminium cylindrical tube subjected to an axial load [44].

In the case of dynamic plastic buckling, the load duration is comparable to the transit time of an elastic wave travelling along the length of the tube. The influence of lateral inertia forces is considerable and favours the development of lateral displacement of the tubes with high mode numbers.

2.1.2 The effects of the geometry of the tube

The mode in which thin-walled structures fail depends strongly on the axial impact velocity and the geometry of the tube.

2.1.2.1 Influence of tube length on collapse mode

Andrews *et al.*[25] investigated the influence of the tube length on the collapse modes of cylindrical tubes subjected to static axial load. These experimental results are shown in Figure 2.7. They indicate that Euler buckling is more likely to occur in tubes with large length to internal diameter, (L/2R), and thickness to internal diameter, (H/2R), ratios.

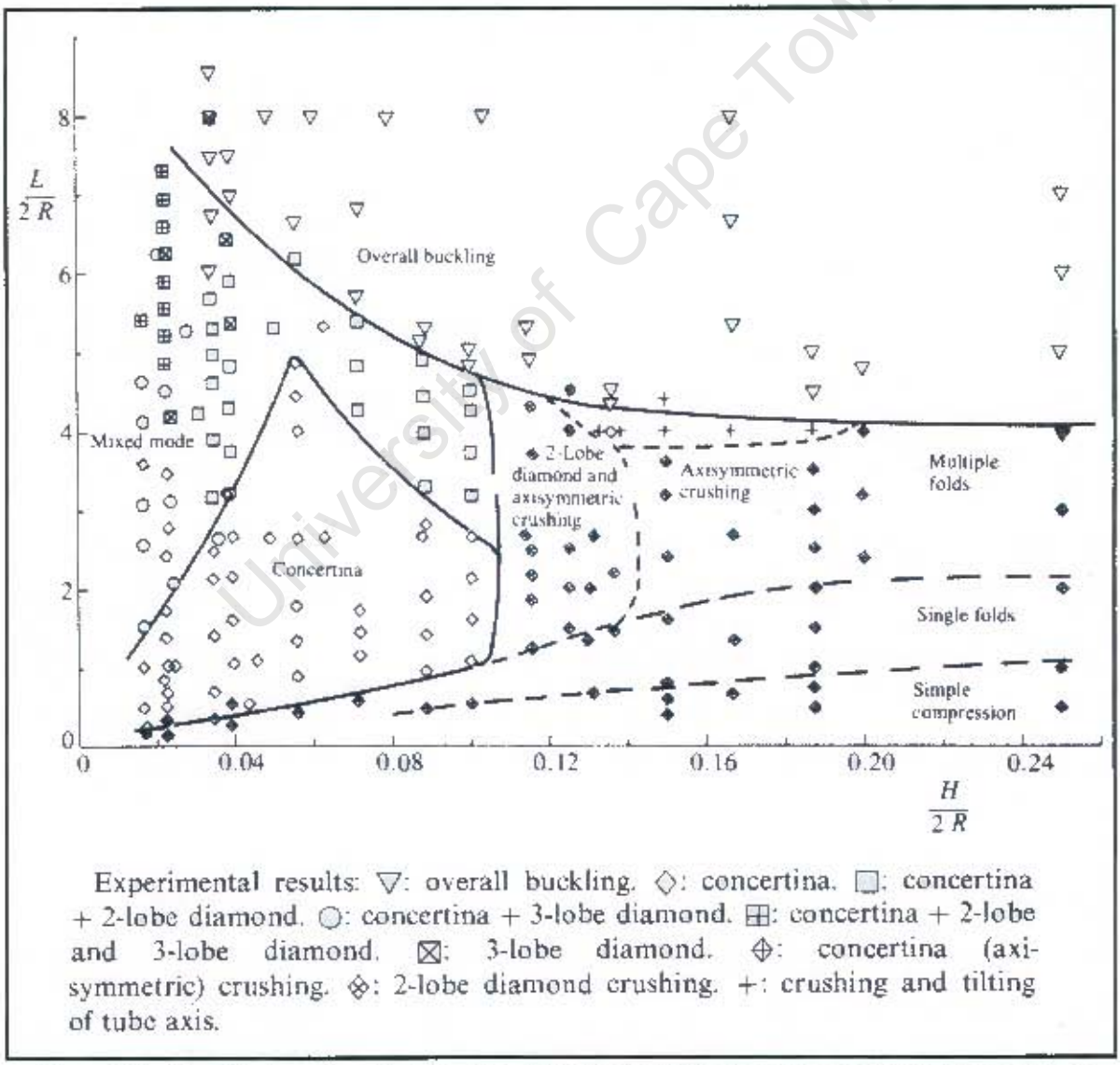

Experimental results: ▽: overall buckling. ◇: concertina. □: concertina + 2-lobe diamond. ○: concertina + 3-lobe diamond. ⊞: concertina + 2-lobe and 3-lobe diamond. ⊠: 3-lobe diamond. ⊕: concertina (axi-symmetric) crushing. ⊗: 2-lobe diamond crushing. +: crushing and tilting of tube axis.

Figure 2.7: Classification chart for collapse modes of thin-walled aluminium alloy cylindrical tubes subjected to static axial loads [25].

Korneck [30]studied the effect of the original tube dimensions on the collapse mode of square tubes loaded axially. The results show a similar trend to that of Andrews et al.[25]. Tubes with large length to width, (L/C), and thickness to width, (H/C), ratios tended to fail in the Euler buckling mode as shown in Figure 2.8.

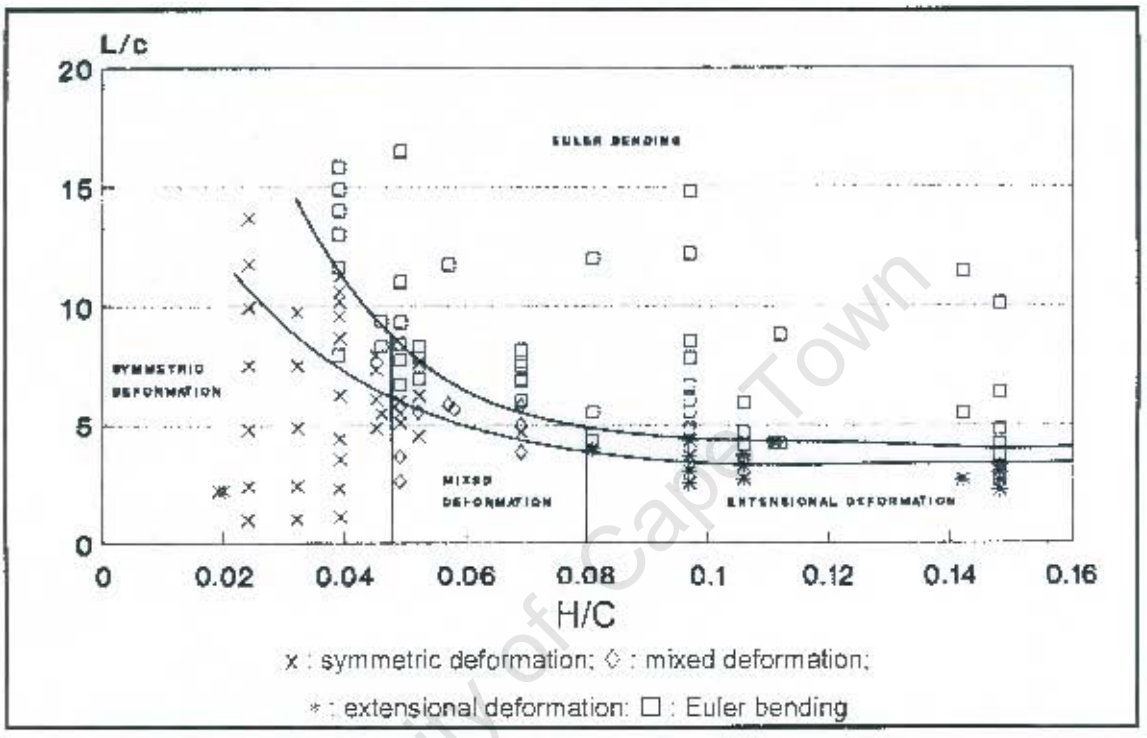

Figure 2.8: Classification chart for collapse modes of thin-walled mild steel square tubes subjected to static axial loads[30].

A long thin-walled tube may suffer an overall (or global) instability, which is an inefficient mode of deformation for an impact energy absorbing system. Abramowicz and Jones[45] studied the role of the geometry of thin-walled tubes loaded axially both statically and dynamically on the transition from inelastic global buckling (Euler buckling mode) to progressive buckling. Square and cylindrical thin-walled mild steel tubes with a range of cross sections and lengths sufficient to encompass both progressive buckling and overall buckling were used. The deformation maps for the square and cylindrical tubes crushed statically and dynamically are illustrated in Figure 2.9 and Figure 2.10. The tube length which marked the transition between progressive buckling and global bending was larger for dynamic impact loadings than for static behaviour.

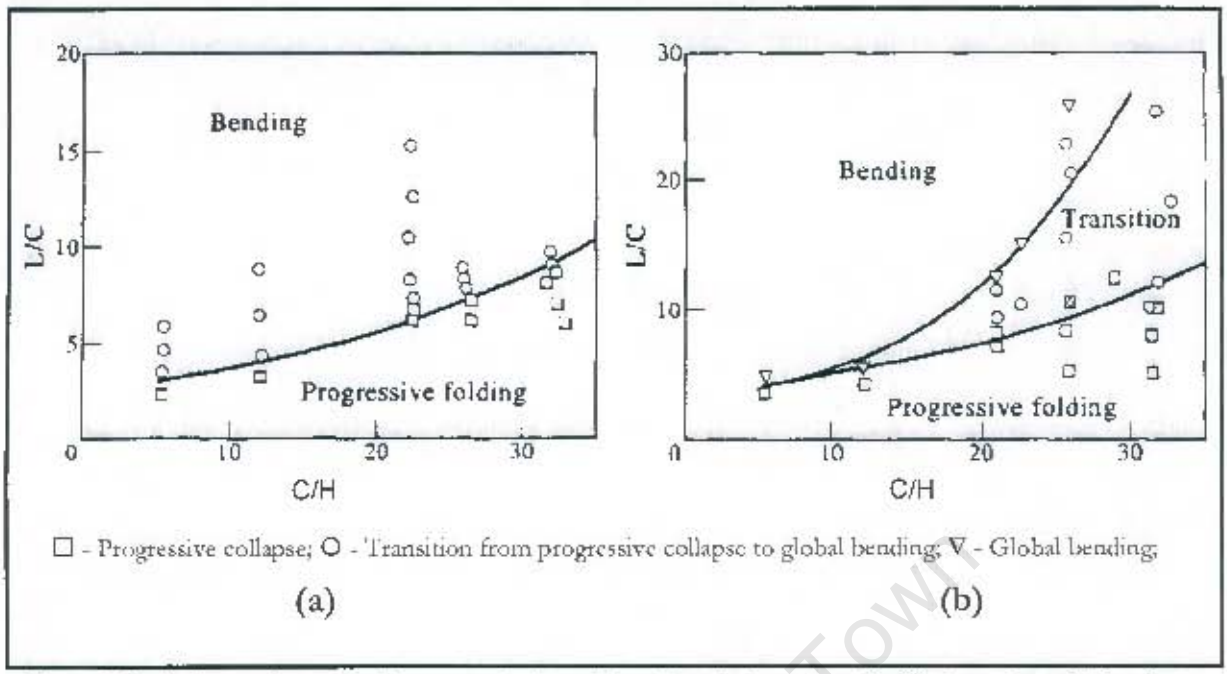

Figure 2.9 : Deformation maps for square tubes subjected to (a) quasi-static (b) dynamic axial loading [45]

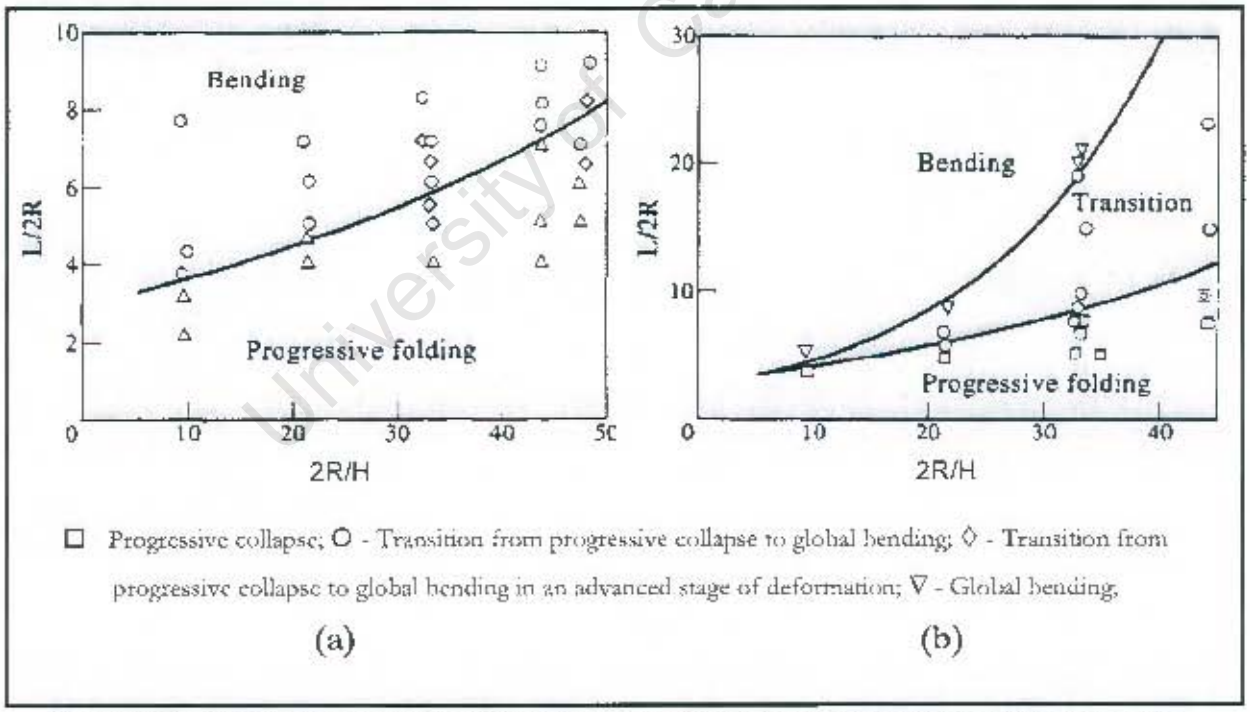

Figure 2.10 : Deformation maps for cylindrical tubes subjected to (a) quasi-static (b) dynamic axial loading [45]

The transition between progressive buckling and global bending was more distinct for static loading of square tubes than for dynamic impact loads. Two distinct collapse modes of progressive buckling and global buckling were observed when the tubes were loaded statically. However, three modes of collapse were observed when loaded dynamically. The tube would either bend without developing a single plastic lobe (Euler buckling mode) or collapse progressively (progressive buckling mode) or bend after developing one or more plastic lobes (transition).

There was a significant range of tube lengths in which the inertia forces promoted progressive crushing and inhibit global buckling. Nevertheless, after a certain lapse of time, the influence of the restraining lateral inertia effects decreased sufficiently for the tube to buckle globally. Thus, the global behaviour of thin-walled tubes was a complex interplay between lateral inertia effects, the axial force (which varies throughout the response) and any change in bending moments produced by global geometry changes[21].

Recently, several authors have explored further the transition between dynamic progressive buckling and global bending of thin-walled tubes. Some experimental data on circular and square stainless steel tubes impacted axially were presented in Hsu and Jones[46] together with the corresponding dynamic material properties. The critical transition lengths were higher than for mild steel tubes which reflect the higher yield and ultimate tensile stresses of the stainless steel. Further experimental data on aluminium alloy 6061 T6 circular cylindrical tubes were reported in Hsu and Jones[47] for impact velocities up to 72m/s.

Dynamic plastic buckling initiated in these relatively thick tubes for impact velocities between 20 and 29m/s compared favourably with the value of 25m/s predicted in Vaughan, cited by [48]. Longer tubes tended to bend globally with a higher mode containing two "global plastic hinges".

Hsu and Jones[49] further investigated the influence of material properties such as strain rate sensitivity and strain hardening, on the mode transitions between progressive buckling and global bending. It was found that the stainless steel tubes absorb the most energy, but were the least efficient for both quasi-static and impact loads.

Karagiozova and Alves [50] conducted experiments on the transition to a global collapse mode of aluminium alloy circular tubes having a single $2R/H$ value and a range of lengths, and axial impact velocities up to 12 m/s. It was observed that the transition occurred up to a length double the corresponding static value. The critical buckling length, which marked the transition between progressive and global buckling of aluminium alloy circular tubes, was significantly influenced by the axial impact velocity.

Jensen *et al.*[43] studied the transition between progressive and global buckling of axially loaded aluminium extrusions in alloy 6060 T6 by quasi-static and dynamic tests. In their series of tests Jensen *et al.*[43] varied the local (width/thickness ratio, C/H = 17.78–40) and global (length/width ratio, L/C = 5–24) slenderness of the extruded members and the impact velocity. In the quasi-static tests and tests that had impact velocity of 13 m/s, the critical global slenderness, referred to as the slenderness where direct global buckling or a transition from progressive to global buckling occurs, was found to be an increasing function of the local slenderness. In contrast, the critical global slenderness was a decreasing function of the local slenderness when the impact velocity was 20m/s.

2.1.2.2 *Effect of thickness/width ratio*

Kim *et al.*[51] conducted a series of experiments to investigate the impact absorption energies of extruded aluminium square tubes. The dynamic compression tests were conducted on three different extruded aluminium tube specimens of thicknesses 1.5, 2.0 and 3.0mm at different strain rates. The size of the plastic folds and the distance between the folds tended to be non-uniform with increasing strain rate. However, the number and shape of plastic folds was constant and stable. The results of the dynamic compression test on extruded tube of varying thickness at the same strain rate showed that the overall area of plastic folds decreased as the thickness increased. Asymmetric folding modes were formed in thinner tubes, while a symmetric folding mode occurred in the thicker tubes. The number of plastic folds decreased as the thickness of the extruded tube increased causing overall bending of the tube.

Further studies by Kim and Lee[52] on extruded aluminium tubes of different shape and width/thickness, (C/H) ratio showed that asymmetric folds were formed mainly in the rectangular tube specimens, as illustrated in Figure 2.11, whereas symmetric folds were formed in the circular tubes. However, symmetric folds were formed in the rectangular specimens with increasing width/thickness ratio and asymmetric folds were formed in the circular tubes with decreasing diameter/thickness ratio.

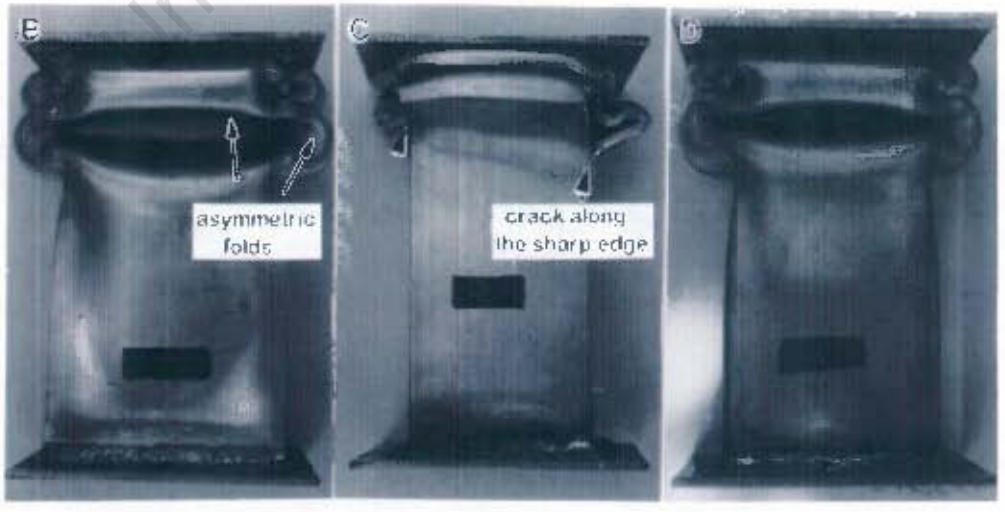

Figure 2.11 : Deformed shaped of extruded aluminium rectangular tube[52].

2.1.3 Effect of material properties

Gupta[53] reported on experiments on both as-received and annealed tubes of aluminium and mild steel and showed that the progressive collapse mode was concertina, diamond, or mixed depending on their state of work hardening, subsequent annealing process and the geometry of the tube. For tubes of diameter/thickness ratios between 10 and 40, it was found that a highly cold worked, as received, aluminium tube deformed in diamond mode and when annealed, it deformed in a ring mode. However, as-received strain-hardened steel tubes deformed in concertina mode and on annealing, deformed in diamond mode, as shown in Figure 2.12. This behaviour was exactly opposite to that of aluminium tubes.

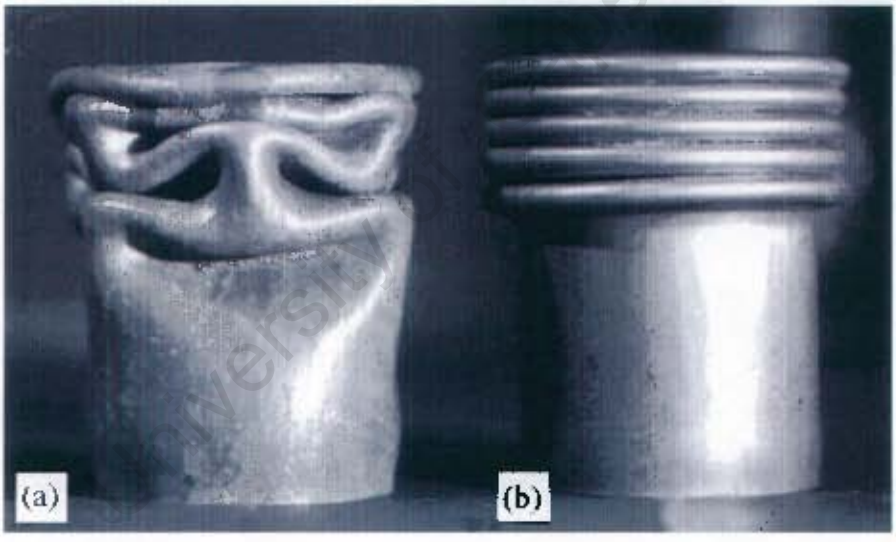

Figure 2.12 : Deformed shape of the 52.6mm diameter steel tube in (a) annealed; and (b) as-received state [53].

2.1.4 Geometric imperfections

As mentioned in section 2.1.1.2, when a tube fails under progressive buckling, the initial peak force is much greater than the subsequent peak (see Figure 2.3). In many instances, these tubes are used to absorb energy in cars and the high force peaks lead to high acceleration on the vehicle occupants during an accident/impact event. As a result, an ideal energy absorbing device, for most cases, should cause a uniform deceleration during the entire stroke. This ideal structure would, in other words, absorb the energy at a constant rate, thus deforming at a constant force throughout the buckling process. A tube which deforms under progressive buckling with an initial peak force equal to the subsequent peak forces would then result in an ideal energy absorbing device which has a linear energy versus displacement curve.

Thornton and Magee[10] showed that collapse initiators, also called triggers, stress concentrators, or imperfections, can be used to:-

- initiate a specific axial collapse mode;
- stabilise the collapse process; and
- for axial crush response, reduce the peak load magnitude or optimise specific crush characteristic.

The use of initiators also sets the start of the collapse process at a specific location on the specimen. These initiators can be either material or geometric modifications to the structure. Examples of material modification initiators are locally annealed regions generated by concentrated heating, or the heat-affected zone generated by a weld. Types of geometric initiators include naturally-formed and mechanically-induced modifications, structural additions or deletions on the component and, for composite components, special end configurations and inserts. The initiators based on geometric modification of the component have the advantages of being visually detectable and controllable by dimension adjustment. The naturally-formed initiators involve pre-buckling of the component past the peak load.

2.1.4.1 Pre-buckle

Langseth *et al.*[54] performed a number of experiments on pre-buckled thin-walled 80mm square aluminium tubes of wall thickness ranging from 1.8mm to 2.5mm. It was found that the number of lobes formed in the tubes with different material properties differed because of the hardening properties of the material. The thinner tubes deformed in a combination of symmetric and asymmetric modes while the thicker tubes (width/wall (C/H) thickness ratio of 32) deformed in the symmetric mode only. This is consistent with work reported by Jones[44].

When crushing pre-buckled tubes, imposed by applying a pre-load to the tube quasi-statically, Langseth *et al.*[54] found that the magnitude of the initial peak force to crush the tube was reduced. Conversely, the total axial deformation was increased compared to an initially straight tube. It was also found that the initial peak force could be controlled by varying the amplitude of the pre-buckle. Airoldi and Janszen[55] adopted a triggering mechanism that pre-buckle the crash tube used as an energy absorbing device to eliminate the initial peak force in the design of a landing gear.

In many actual situations where the tubes are used as energy absorbers, the force may be applied obliquely to the tube. As a result, the tube may buckle in the Euler mode rather than the progressive buckling mode. It has been found that by including a pre-dent or geometric imperfection in the tubes, the structures are forced to follow the shape of the imperfections when loaded axially[56]. Hence, a tube can be forced to deform in a particular mode of failure by including geometric imperfections in the tubular structure even if the geometry of the tube would normally cause it to deform in another mode of failure.

2.1.4.2 Sharp corner indentations

Corner cutouts are commonly used mechanically-induced imperfections for square tubes. Abah *et al.*[57] had employed cut-outs to initiate collapse and reduce the peak load. Schriever and Helling [cited in 19] conducted a series of tests on square tubes with sharp dents along the corners of the tube at different distances apart. The dents were characterised by their depth and included angle.

The ideal distance between the dents along the length of the tubes was found to be half the natural wavelength of the tube and the peak force was reduced by approximately 17% and the mean crushing force decreased by 10%. The geometric efficiency increased by 7% compared to the total energy absorbed by an un-dented structure over the entire stroke. If the imperfections were placed closer together along the length of the tube the stability of the collapse mode was lost.

It was also found that while un-dented tubes tended to fail in the Euler buckling mode when the force was applied at an angle of up to 5.5° to the longitudinal axis of the tube, the dented tube underwent progressive buckling under the same conditions.

2.1.4.3 Parallel indentations in the side of the tubes

Sharp dents

Komecki[30] studied the effect of side dents on the crumpling characteristics of the tubes. A 90° angle indenter was used to create the one or two dents opposing each other on both sides of mild steel square tubes. Figure 2.13 shows the final deformed shape of dynamically loaded pre-dented square tubes.

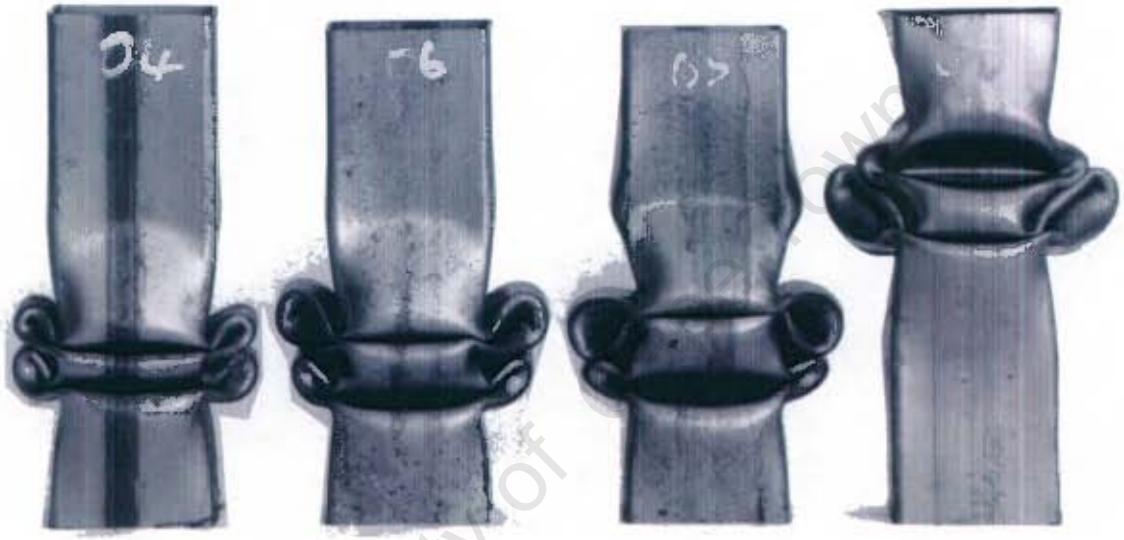

Figure 2.13 : Symmetric deformation of dynamically loaded pre-dented square specimens – Dent depth increases from left to right [30]

As expected, the pre-dented tube crumpled with a decreased initial peak load. This pre-dent, however, did appear to affect the other buckling characteristics of the tube significantly. The tubes stabilised into the normal progressive mode when the third lobe was formed. Further tests were performed to investigate the effect of the depth of the side dent on the initial peak force. Consequently, an optimum dent depth was approximated as the depth at which the initial peak force is equal to the third peak load in magnitude assuming that the third peak force could be used as the average magnitude of the high peak load. Figure 2.14 shows this relationship for 50mm square tubes of wall thickness 1.2mm.

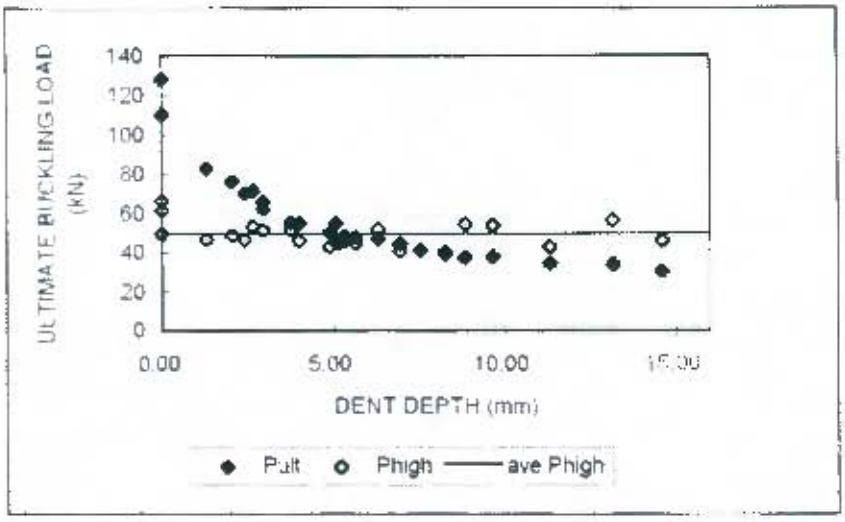

Figure 2.14 : Optimum dent depth for mild steel square tubes of width 50mm and wall thickness 1.2mm [30]
(Pult : ultimate buckling force, Phigh : high peak force, ave Phigh : average high peak force)

Dynamic tests on similarly prepared specimens, using a drop hammer with a maximum trolley mass of 58.6kg and a maximum height of 4.5m, showed that the folding geometry remained unchanged with an increase strain rate. The mean collapse load, however, increased.

Cylindrical dents

Marshall and Nurick[33, 34] studied the effect of cylindrical side dents of diameter ranging from 2mm to 50mm on the progressive buckling of thin-walled square tubes. The results of the parallel cylindrical indentations on the ultimate buckling load of the tubes illustrated in Figure 2.15 showed that the ultimate buckling load decreases with increasing severity of the indentation. The mean crushing load and the ultimate buckling load were unaffected by the depth and size of the indent. Nonetheless, the dents affected the shape of the first lobe during the collapse process. An increase in the depth of the indentations resulted in an increase in the size of the first lobe. If the dent was sufficiently large so that the opposite sides of the tube touched, a very large first lobe was created and the tube bent over. Tubes indented using a 50mm diameter cylinder and crushed quasi-statically are shown in Figure 2.16. These specimens demonstrate the increase in size of the first lobe with an increase in the depth of the indentation.

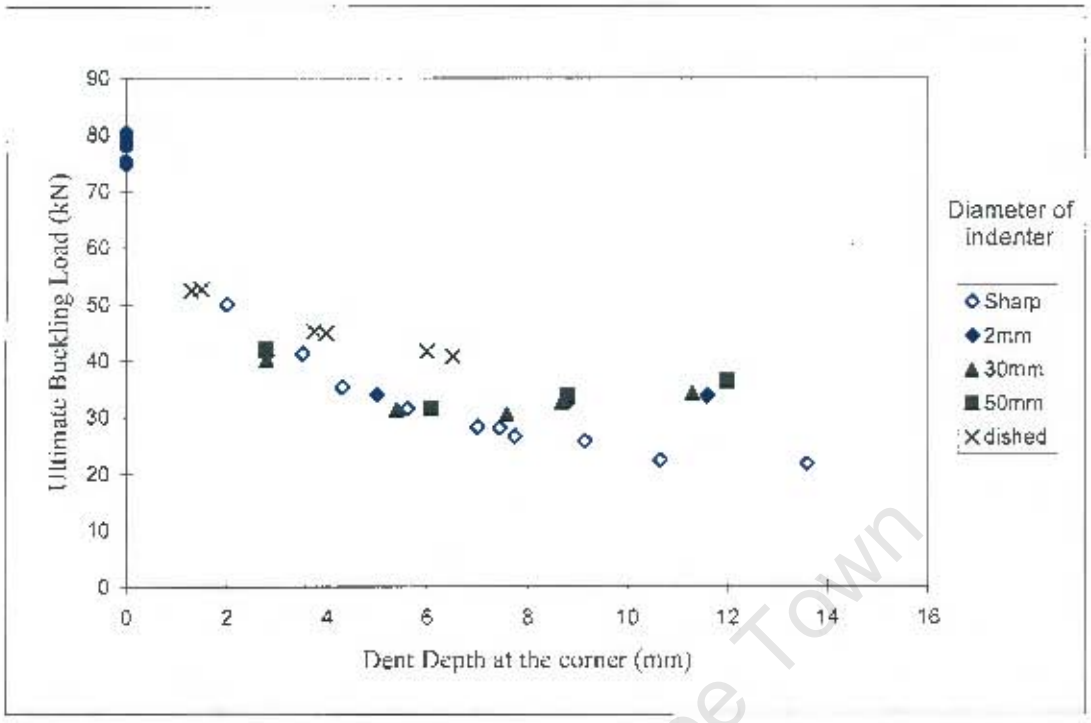

Figure 2.15 : The effect of opposing parallel indentations and opposing dished indentations on the ultimate buckling load [34]

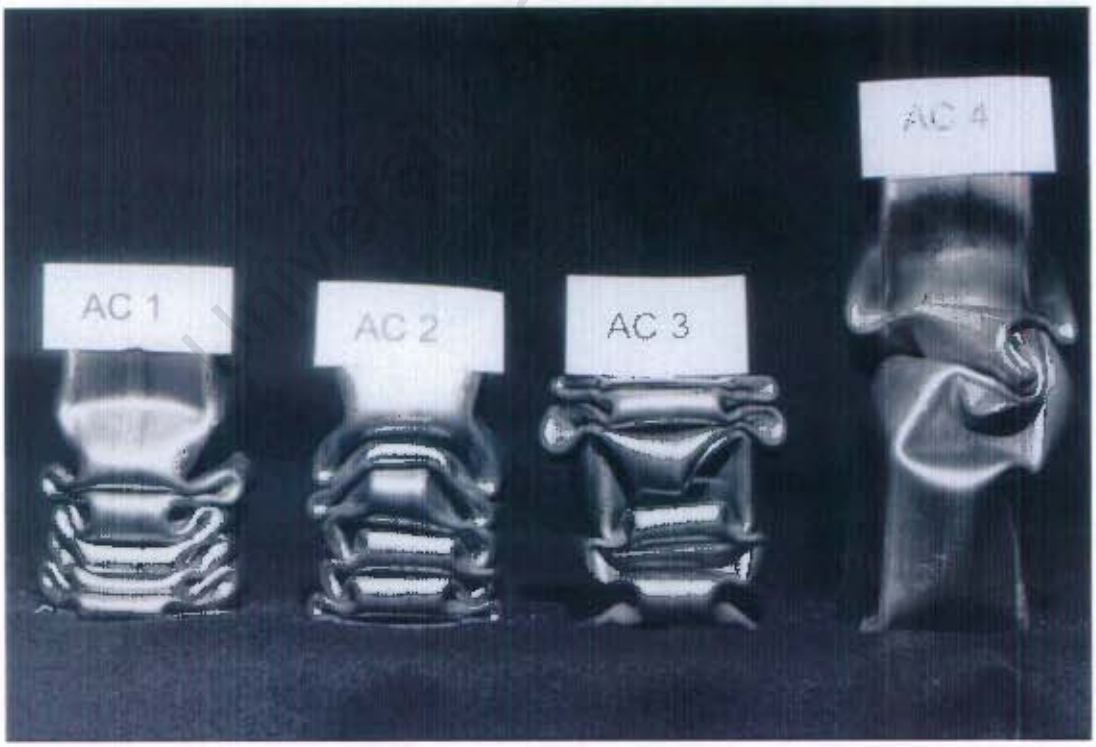

Figure 2.16 : Quasi-statically crushed square tubes with opposing parallel cylindrical indentations [34] (depth of indentations increases from left to right)

Dished indentations

Marshall and Nurick[33, 34] also investigated the effect of dished indentations on the progressive buckling of square tubes. The dished indentations, produced using a hemispherical indenter, were deeper in the centre than at the corner of the tube. The results of the depth of the indentations at the corner of the tube on the ultimate buckling load are shown in Figure 2.17. The effect of the dished indentations on the ultimate buckling load was less than that of parallel indentations. However, a similar but more exaggerated trend than that of indentations formed by cylindrical indenters was observed when the dished indented tube was crushed. The effect on the stability of the symmetric buckling is shown in Figure 2.18. The size of the first lobe increased with an increase in the depth of the indentation. The opposite walls of the tube met when the first lobe was developed, thus preventing the full formation of the lobe. The effective stroke of the tube was, therefore, significantly decreased.

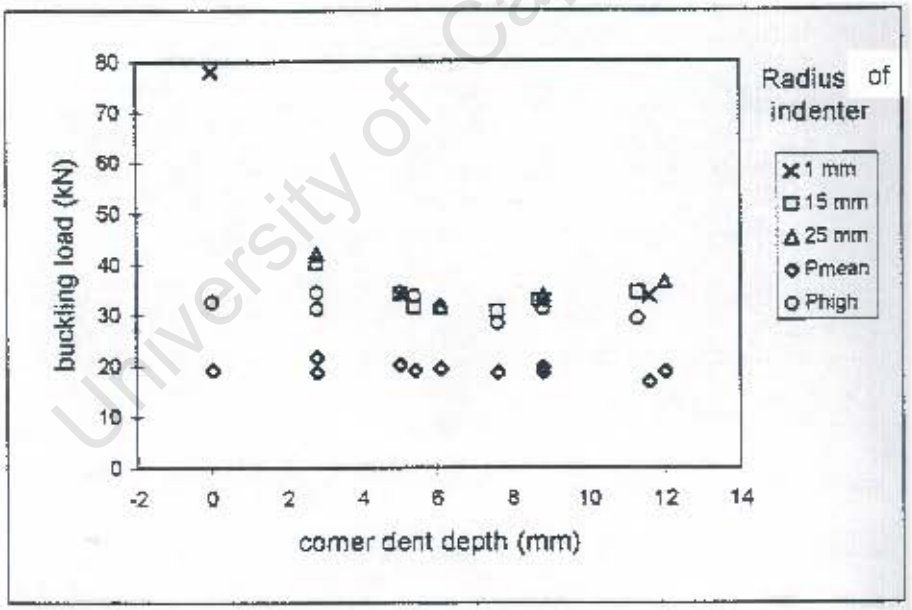

Figure 2.17 : The effect of the depth of the corner dent on the Ultimate Buckling Load [33].

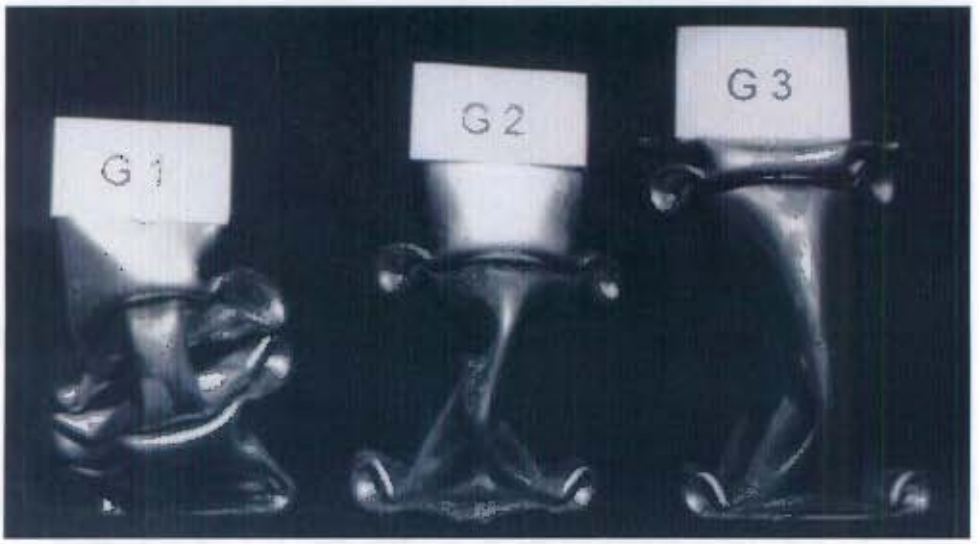

Figure 2.18 : Quasi-statically collapsed square tubes with opposing dished indentations [34] (The indentations were induced with a hemispherical indenter of radius 100mm and the depth of indentations increases from left to right)

Triggering dent

Lee *et al.*[35] studied the effect of triggering dents on the energy absorption capacity of quasi-statically compressed aluminium tubes. The tubes were 50x50mm in cross-section, 300mm in length and 2mm in thickness. Two types of dents, full-dent and half-dent as shown in Figure 2.19, were introduced at the folding sites pre-estimated by computer simulations. The results showed that the first peak load decreased with the introduction of the dents. The half-dented specimens exhibited the same number of plastic hinges as the full-dented tubes. However, the crushing force required for the formation of each hinge was increased thereby increasing energy absorption capability. When the triggering dents of the same interval were introduced without consideration of the peak location of the folding wave, inhomogeneous deformation, together with overall bending occurred.

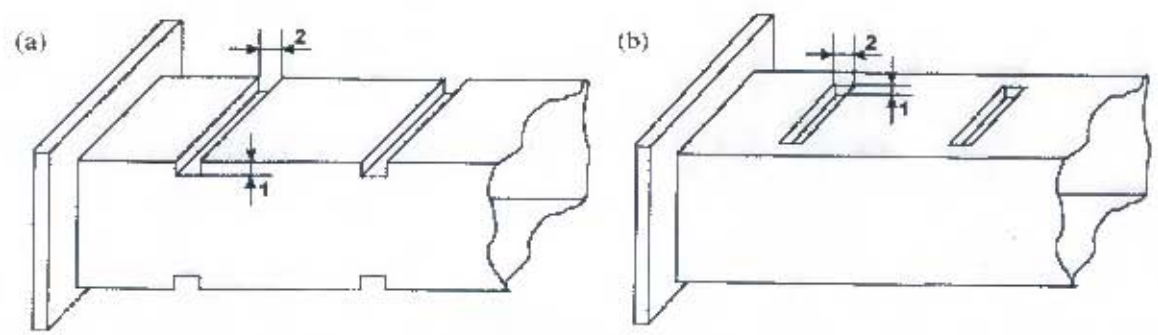

Figure 2.19 : Shape of (a) full-dent and (b) half-dent introduced into the aluminium tube specimen [35].

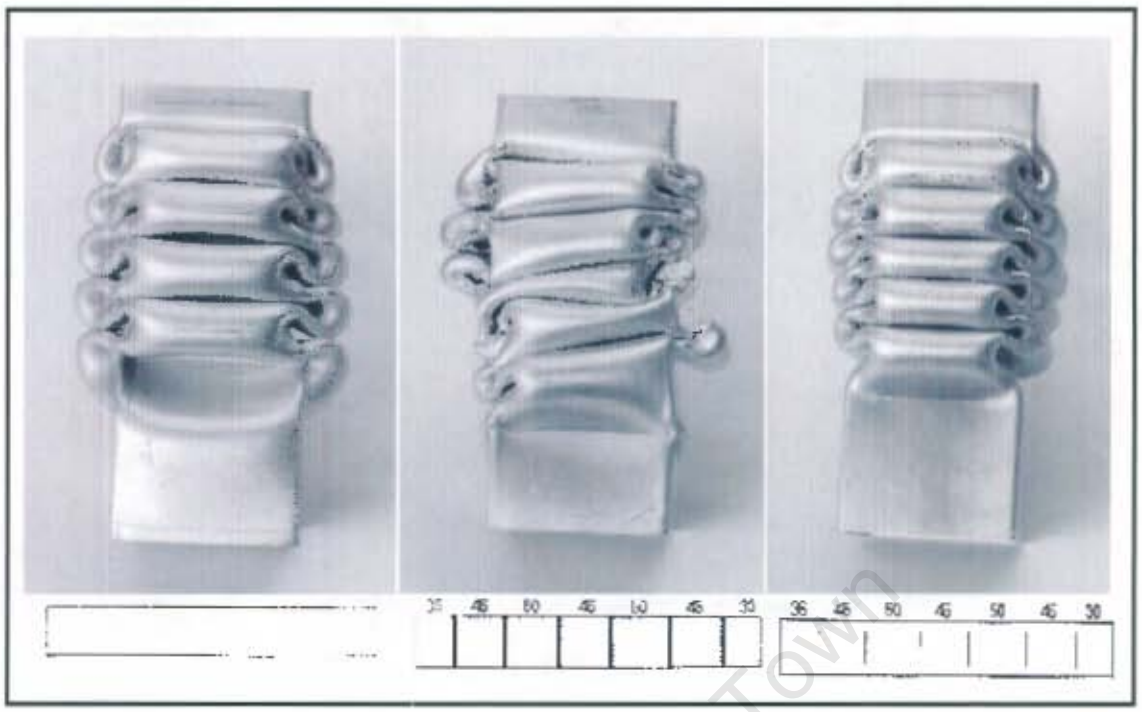

Figure 2.20 : Deformed aluminium tubes with schematic of the locations of triggering dent [35].

DiPaolo *et al.* [58]used a double set of machined full width grooves of different depth in opposite sidewalls with vertical offset (see Figure 2.21) to demonstrate the ability to restrict symmetric axial crush mode response to a specific configuration.

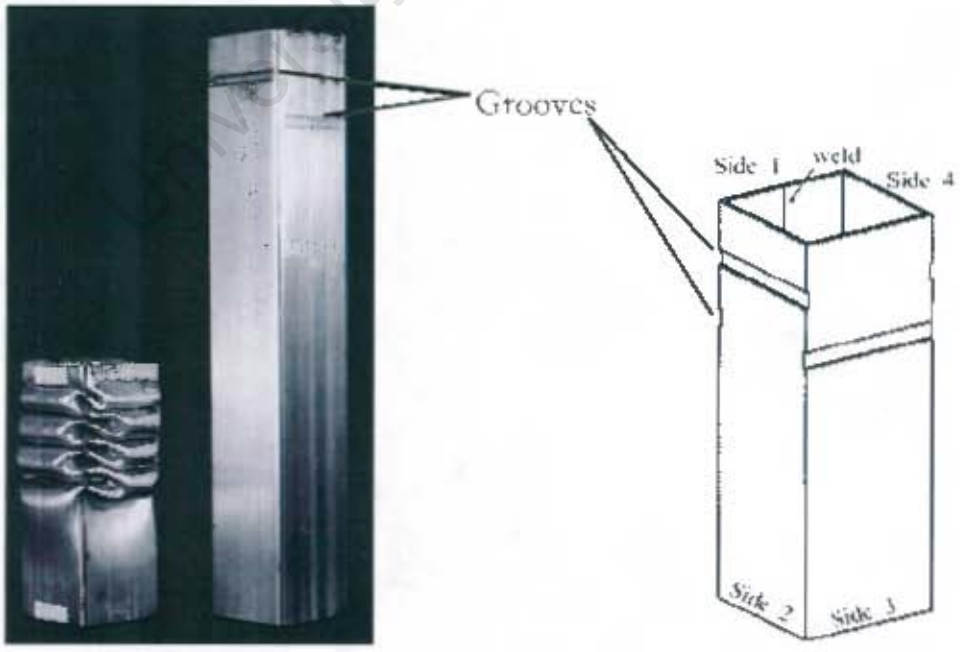

Figure 2.21 : Symmetric axial crush response mode—ductile metallic alloy: axial crush specimen and un-deformed tube [58].

Sigalas *et al.*[59] made use of chamfer-based trigger mechanisms to study the energy-absorbing capabilities of glass fibre/epoxy composite tubes. Tubes with external chamfers ranging from 10° to 90° were crushed to different extents and the resulting microstructures were examined microscopically. It was found that, for this material, the crushing process was usually initiated by local bending of the chamfered parts of the tubes and by internal cracking. These events gave rise to the generation of wedges of crushed material which were pushed to the inside of the tube wall. The stresses generated at the root of the wedge gave rise to lateral cracks, which caused small rings of material to be sheared off. This sequence of events dominated the initial stages of the crushing process. At a later stage, the mode of crushing changed to one of frond-wedge-frond geometry.

Mamalis et al. [60] also reported on the crumpling of thin-walled grooved tubes. They examined PVC and steel tubes with two kinds of groove patterns; external circumferential grooves and internal axial grooves and reported on the non-axisymmetric diamond mode of deformation in both cases. Collapse was initiated at the thinnest section of the tube (groove) and spread along the various rings and grooves.

Other studies that investigate the effects of grooves on the crashworthiness characteristics of thin-walled tubes under axial compression include the work by Hosseinipour and Daneshi [37, 61-63]. Annular grooves cut were introduced alternately inside and outside the tubes surfaces with various distances, in cylindrical tube to force the plastic deformation to occur at predetermined intervals with the aims to improving the uniformity of the load–displacement behaviour and predicting energy absorption capacity of the tubes.

Corrugated tubes

Other physical modifications have been used to control specimen performance in both the initial and the secondary phases of axial crush. Types of these initiators-controllers include: corrugations formed in "square" tubular sections by Thornton and Dharan[64] and a series of machined circumferential grooves in right circular cylindrical tubes by Mamalis *et al.*[65].

Singace and El-Sobky[66] studied the energy absorption characteristics of corrugated aluminium and PVC tubes. Corrugations were introduced in the tube to force the plastic deformation to occur at predetermined intervals along the tube generator. The experiments were also performed to investigate the effect of heat treatment, filling of the tube core with foam and corrugation on the tube performance as an energy absorption element. Straight tubes were used to provide a means of comparison. The corrugated tubes always deformed into the concertina mode irrespective of the heat treatment. Nevertheless, the heat treatment reduced the overall wave amplitude decreasing the difference between the highest (or the lowest) load and the mean load. Figure 2.22 shows the load-displacement behaviour for both annealed and non-annealed corrugated tubes under axial load. Annealing the corrugated tubes decreases the difference between the mean collapse load, a property that is favourable in an efficient energy absorption device. However, such action reduced the overall specific energy absorbed by the tubes. Filling the corrugated tube core with polyurethane foam (density 50kgm^{-3}) improved the amplitude of the mean load but does not change the overall behaviour. Crushing of corrugated tubes with different corrugation depths showed that tubes with shallower corrugations exhibited behaviour approaching that of the straight tubes. Tubes with a corrugation depth to radius ratio of about 0.12 produced better load-deformation response and uniform collapse load. Axial crushing of corrugated PVC tubes showed similar properties to the metal tubes, i.e. elimination of the overall elastic stiffness.

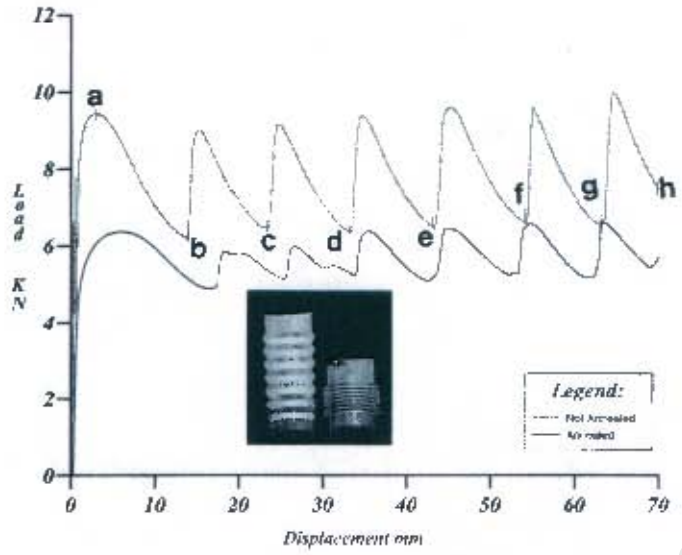

Figure 2.22 : A typical load-displacement characteristics of aluminium alloy corrugated tubes [66]

2.1.4.4 Circular cut-outs

Gupta *et al.* [32, 67] carried out tests on aluminium and mild steel tubes of different diameters, lengths and wall thicknesses. Cut-outs in the form of circular holes, varying in diameter, number and position were laterally drilled in the tubes. In tubes where the holes were located in parallel positions, deformation was initiated at the location of the holes at one of the planes. The tubes, with holes in cross positions, deformed in such a way that the axis of symmetry of deformations was rotated by 90°. The presence of the holes in the tubes was found to reduce the first peak load and alter the mode of collapse and, as a consequence, could be used to avoid Euler buckling when relatively long tubes were crushed.

Numerous experimental studies on the effect of cut-outs on the peak load of axially compressed cylinders have been reported by Toda[29], Kormi *et al.*[31] and Gupta and Gupta[32]. The ultimate buckling load was found to be governed by the parameter:-

$$\alpha = \frac{a}{\sqrt{RH}}$$

where a : characteristic cut-out dimension, R : cylinder radius and H : wall thickness.

Listed below is a summary of the results of the experiments on polyester cylinders obtained by Toda[29].

$\alpha \leq 1.0$	the cut out had no appreciable effect
$1.0 < \alpha < 2.0$	there was a sharp decrease in ultimate buckling load with an increase in α
$\alpha > 2.0$	there was a small decrease in the ultimate buckling load with an increase in α

Surko[56], Meng *et al.*[68] and Li *et al.*[69] used the fact that a square tube can be approximated by four flat plates to analyse the crushing of tube of rectangular cross section. The von Karman principle was used to simplify the elastic plastic analysis of thin plates with a centrally positioned circular hole.
Surko[56] described the von Karman effective width as:

$$b_e = 1.9H\sqrt{\frac{E}{\sigma_y}},$$

which means that if the diameter of the hole is smaller than

$$\phi \leq C - 1.9H\sqrt{\frac{E}{\sigma_y}}$$

then the hole should have little or no effect on the buckling characteristics of the plate.

Marshall[33, 34] performed experiments on square thin-walled tubes of width 50mm and wall thickness 1.2mm with two holes drilled into the opposite faces of the tubes. The diameter of the holes was varied from 16mm to 38mm. Similar observations, to that of Gupta *et al.*[32, 67] for cylindrical tubes, were identified. The square tubes started to collapse at the hole with a decrease in the ultimate buckling load. For tubes, with cut-out diameters of less than 32mm, the mean and subsequent peak force did not differ from that for a tube without imperfections as the tube buckles progressively.

Specimens with holes of greater than 32mm tore rather than buckled progressively. The introduction of the hole also affected the formation of the first lobe. An increase in the diameter of the holes caused a decrease in the size of the first lobe as illustrated in Figure 2.23. Consequently a decrease in the size of the first lobe causes instability in the buckling mode as subsequent lobes formed skew.

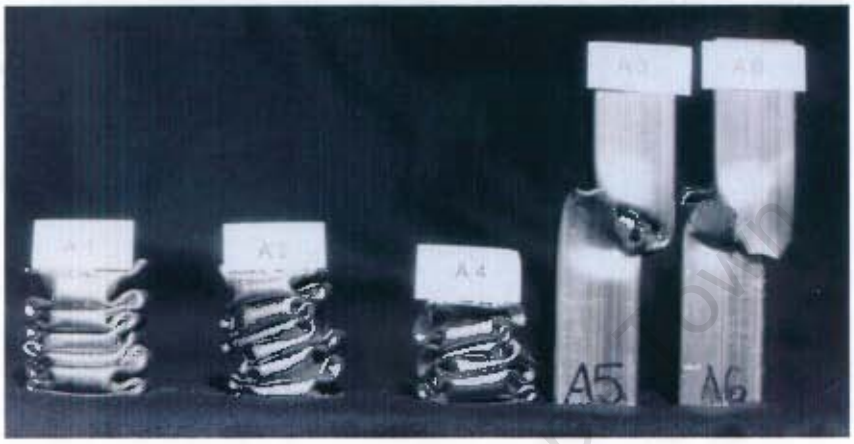

Figure 2.23 : Quasi-Statically crushed square tubes with two opposing holes [34] (diameter of the holes increases from left to right – it appears that the size of the first lobe decreases with increasing hole diameter until tearing occurs)

Arnold and Alhentof[70] also carried out similar tests on square tubes made out of 6061 T4 and T6 aluminium alloy. They found that the material properties, specifically hardening capacity and ductility have a significant effect on the collapse mode and energy absorption. A greater amount of energy was absorbed by the more ductile material.

Cheng *et al.*[71] found that different geometrical cut-outs, namely circular, elliptical and slotted through holes (major axis 7.14, 10.72 and 14.29mm with aspect ratios 1, 1.33, 2.0 and 3.0), initiated a splitting and cutting mode of deformation for square AA6061-T6 tubes (200mm in length, 38.1mm in width and 3.15mm thick) rather than global bending. The hole cut-outs reduced the peak crush load and increased the total energy absorbed. For the 7.14mm cut-outs, the imperfections did not affect the peak crush load and the total energy absorbed. Geometrical influence was observed in cases where the major axes of the cut-outs were 10.72 and 14.29mm with an aspect ratio of 3.

2.1.4.5 Combined structural deformations

Surko[56] performed limited experiments to study the effect of combined structural imperfections on the ultimate buckling load and collapse mode of box columns. The mild steel box columns specimens were constructed of four 140mm square side plates with length to thickness ratio of 88 with two rigid end plates. The imperfections represented different possible modes of initial lateral deflection. The deformation shapes were a pyramidal bulge from the corners outwards to the centre of the side, and an outward concertina shaped bulge which resembled the extensional mode of progressive buckling. Each specimen was built with a central hole on each face.

The geometrically-perfect box column specimen used as a baseline buckled in the asymmetrical mode (opposite sides folded in or out together), while the partially damaged specimens buckled symmetrically with curved folds near the mid-plate. Dishing of the order of 5 – 15 plate thicknesses reduced the peak load by approximately 15 – 35%. The mean crush load was not significantly changed although this aspect was not completely covered as the box columns were crushed to between 14% and 50% of their original length. The effect of the holes on the peak load was minimal.

Marshall[33, 34] conducted a series of experiments on square thin-walled tubes with combined imperfections. The imperfections were induced by first drilling a hole and subsequently indenting the tube with a hemispherical indenter positioned symmetrically above the hole. The combination of holes and dents had a greater effect on the ultimate buckling load than either holes or indentations acting individually. There was, however, no significant difference in the mean buckling load. The effect of the combined imperfections with respect to depth of the indentation at the corners of the tube is plotted in Figure 2.24.

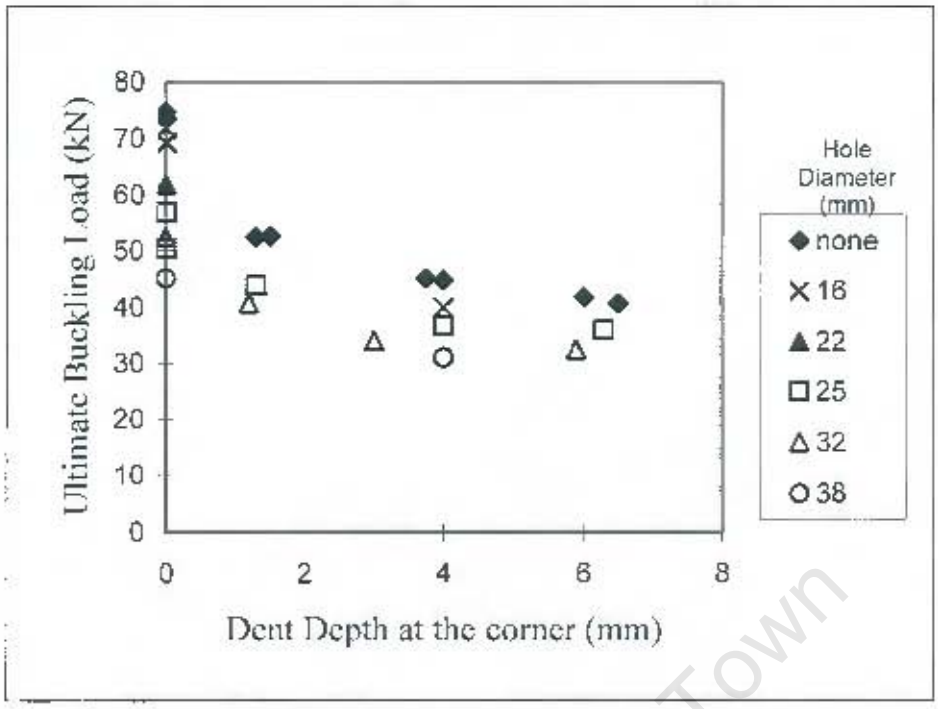

Figure 2.24 : The effect of the depth of dished indentations on ultimate buckling load of specimens with opposing combined imperfections [34]
(diameter of hole 32mm, depth of indentations increases form left to right)

Specimens with indentations depth of 3.5-4mm and holes with diameters increasing in size from left to right are shown in Figure 2.25. Tubes with small holes had a large first lobe while tubes with large holes had a smaller first lobe. This indicated that there is a large range of imperfection dimensions that achieve an adequate first lobe size for stable symmetric progressive buckling.

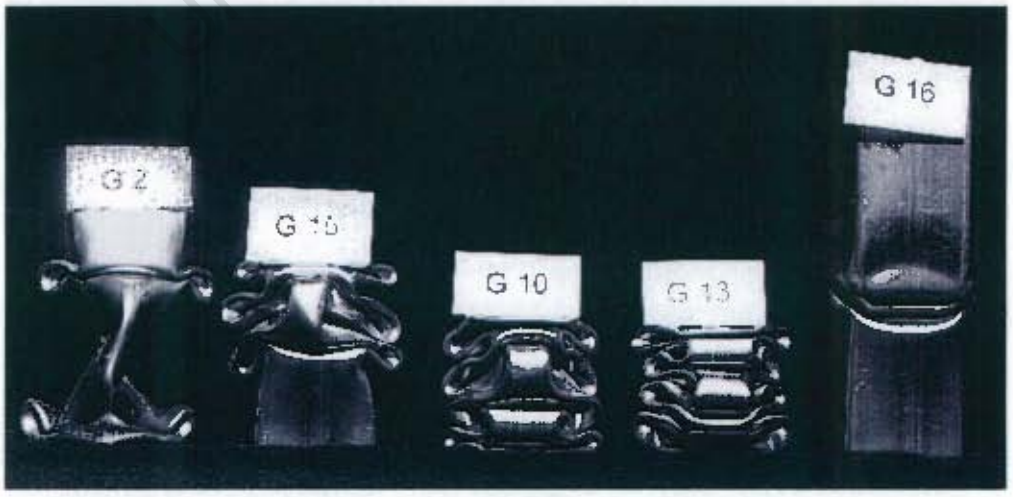

Figure 2.25 : The effect of the diameter of the holes on ultimate buckling load of specimens with opposing combined imperfections [34]
(indentations depth 3.5-4mm, diameter of hole increases from left to right, G2 has no hole)

Specimens with 32mm holes and indentations increasing in depth from left to right are shown in Figure 2.26. For small dent depth (1.5mm) the first lobe in the specimen appeared to be smaller than the natural lobe size. The first lobe size was influenced more by the large hole than the small indentations, while the distance between the plastic hinges was dominated by the dent depth length.

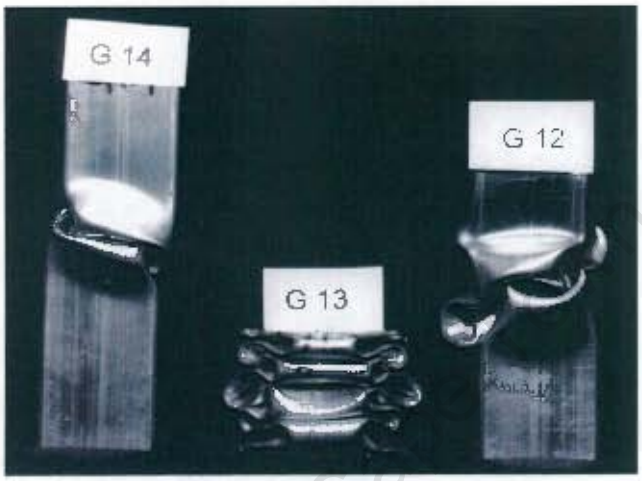

Figure 2.26 : The effect of the depth of dished indentations on ultimate buckling load of specimens with opposing combined imperfections [34]
(hole diameter : 32mm, depth of indentations increases from left to right)

2.1.4.6 Stiffened tubes

Structural stiffening is frequently used to increase the strength of a structure. In the case of square or circular tubes, it is possible to induce a highly undesirable mode of collapse (from an energy absorption viewpoint) if the geometry of the tube is incorrect. A number of experimental studies have been performed to obtain the axial collapse behaviour of stiffened structures, for instance Kormi *et al.*[72], and Jones *et al.*[73-75] . Common examples of stiffened tubes are the top-hat and double-hat sections which are widely used in the automotive industries. Numerous studies on the static and dynamic axial crushing of the top-hat structures have been reported in the literature, for example Refs [76-79]. White and Jones[76, 77] assessed the influence of several design and crashworthy parameters on the static collapse behaviour of thin-walled top-hat and double-hat section structures both

experimentally and theoretically. An increase in size of the external flange of the top-hat sections (from 10 to 25mm) improved the collapse regularity for the thin-walled sections. The increase in flange width also increased the mean loads and axial displacement before instability occurred. The top-hat sections deformed into a more regular progressive buckling compared to the double-hat sections. However, the double-hat sections collapsed with a higher mean load suggesting better capabilities to absorb more energy provided the collapse mode was progressive buckling. Figure 2.27 shows the typical collapse profile for a spot-welded top hat sections.

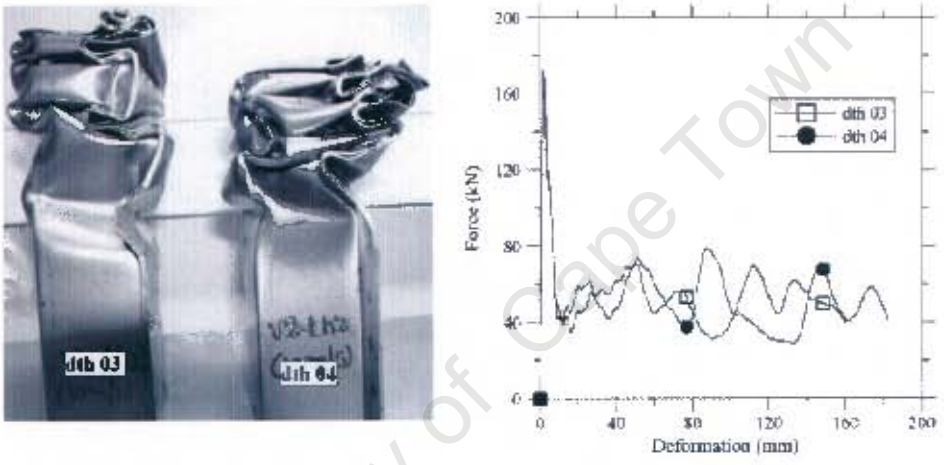

Figure 2.27 : Collapse profiles and load – deformation history of a spot-welded top-hat sections after impact testing at 10m/s[79]

Lee *et al.*[80] compared the crashworthiness of double-hat shaped section made from dissimilar materials (aluminium and steel) using self-piercing rivet and adhesive bonding to steel sections joined by spot weld. The self-piercing rivet joined sections absorbed more energy than the adhesive-bonded section. The specific energy absorbed and the deformed length of the dissimilar section member were higher than that of steel. The mean crush load and ultimate peak load of the dissimilar section member were also lower than the spot welded steel sections. Consequently, Lee *et al.*[80] suggested that the self-piercing rivet joining method could be use as a substitute for spot welding.

2.1.4.7 *Foam-filled tubes*

Another form of stiffened tubes is filled tubes. Tubes can be filled with cellular structures such as honeycombs, wood and foams and used for energy absorption devices. The compression characteristics of these materials, besides their mass efficiency, show that they approach an ideal energy absorber. According to Thornton and Dharan[64] and Gibson and Ashby[81], the cellular materials offer a distinct plateau of almost constant stress in the uni-axial compression stress-strain curve up to nominal strain values of 70-80%. Figure 2.28 illustrates typical foam filled specimens and material behaviour for aluminium extrusion in uni-axial tensile and aluminium foam in uni-axial compression.

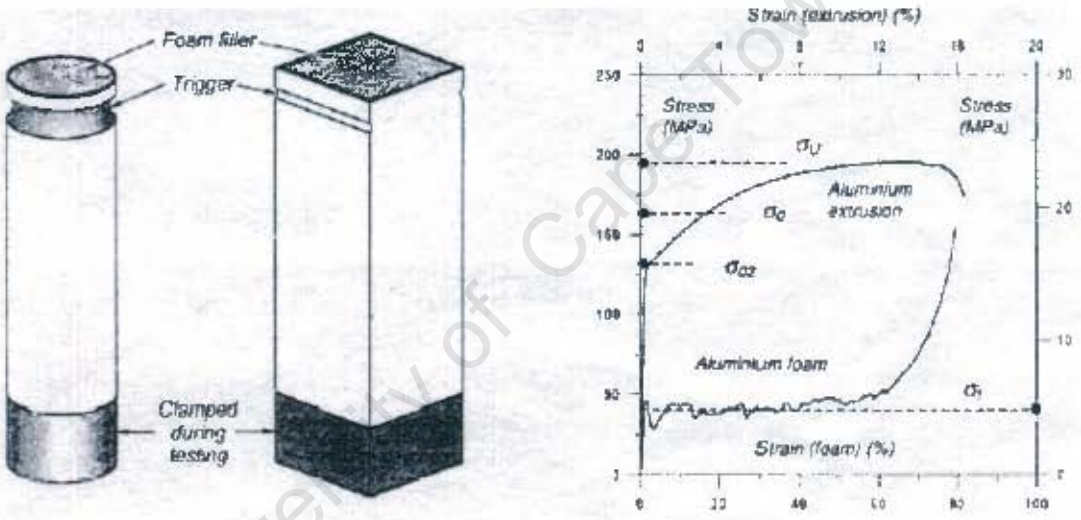

Figure 2.28 : Test foam filled specimen geometry & typical material behaviour [82]

The blend of tubular members and cellular filler material combines the crushing energy of both types of structures which seem to be efficient with the filler material providing enhancements to the empty tube. The compression of the filler material and its interaction with the tube lead to higher energy dissipation provided the tube buckles progressively.

Many studies have been carried out to investigate the effects of different fillers on the performance of energy absorption systems. The crashworthiness performance of a tubular structure due to inclusion of polyurethane foam has been investigated. For instance, Reddy and Wall[83] presented results of static and dynamic tests on very

thin circular metal tubes, which were filled with low density polyurethane foam. The presence of the filler material did not only 'stabilise' the almost irregular buckling pattern of the empty cylinders, but also improved the energy absorption efficiency. The mode of deformation of the tube was found to change from irregular diamond crumpling to axi-symmetric bellows folding due to the fillet.

Toksoy and Güden[84] investigated the strengthening effect of polystyrene foam filling in thin-walled aluminium circular tubes. The polystyrene foam affected the deformation mode. Empty tubes of different diameters; 16 and 25mm; deformed in diamond mode. Foam filling changed the deformation mode to concertina in 25mm diameter tube due to thickening effect of foam filling.

Thornton[85] examined the collapse of foam-filled tubular structures of different cross-sections and concluded that irrespective of the enhancement in the overall strength of the structure, the foam is not weight-effective and, instead, using thicker tubes would be more energy efficient. Lampinen and Jeryan[86] experimentally studied the behaviour of foam and found that although the common mode of failure of foam-filled tubes was progressive collapse, over-dense tubes would tend to collapse in Euler mode. It was concluded that foam plays a major role in the stability of deformation of tubular struts. Reid *et al.*[87] investigated the collapse of foam-filled thin-walled metal tubes under quasi-static and dynamic conditions. It was concluded that the tubing outer skin interacted with the deformation of the foam and that, in the presence of foam of proper density, very thin tubing tended to collapse in a more axi-symmetric mode of deformation. They found that the mean crushing load and the collapse folding length were dependent upon the foam density. Abramowicz and Wierzbicki[88] and Ashby *et al.*[89-91], in their investigations on foams and other cellular filling materials, came to similar conclusions on the influence of foam density.

Low-density foam-like metals have been introduced into the cost and weight effective design of energy absorption systems, according to Kunze *et al.*[92]. Santosa and Wierzbicki[93] found that filling prismatic columns with low-density aluminium foam significantly enhanced the structural bending strength and that it was a better alternative to the thickening of the column wall. Hanssen *et al.*[82, 94-99] carried out quasi-static experimental investigations on aluminium foam-filled square extrusions and concluded that properly bonded foam produces specific energy higher than non-bonded foam-filled extrusions. In addition to extensive experimental results, simple relations between parameters which were likely to influence the crushing behaviour of such composite structures, and design formulas were presented.

Examples of final deformed shapes in axial crushing of some square and circular extrusions are shown in Figure 2.29. The foam filler was found to have significant effect on the deformation behaviour of the tubes. It caused the square extrusions to develop more lobes and for a critical foam filler density, the deformation behaviour changed from diamond to concertina mode[95, 96].

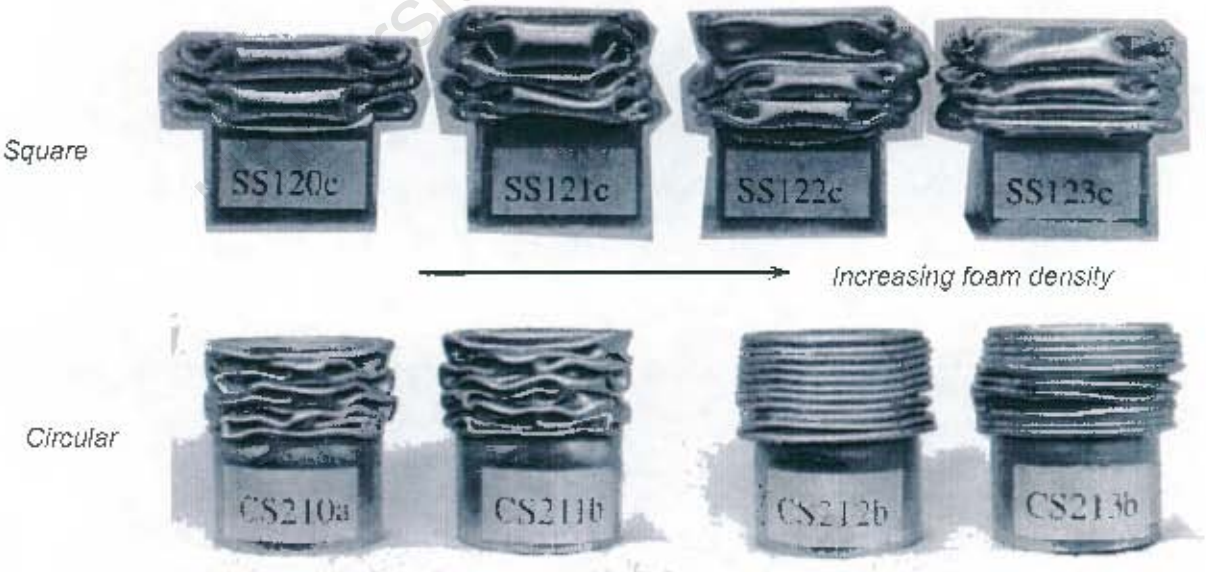

Figure 2.29 : Deformation behaviour of square and circular extrusions as a function of foam filler density [95, 96]

Seitzberger *et al.*[100] have shown experimentally and numerically, that filling square steel tubes with aluminium foam may considerably improve their mass efficiency with respect to the mean forces, provided that the buckling modes of the tubes remained progressive. Santosa and Wierzbicki[101] used the finite element method for numerically studying filled tubes and also reported on efficiency improvements of axially compressed square aluminium tubes, which were filled with honeycomb or foam.

Seitzberger et al.[100, 102] carried out quasi-static experiments on monotubal (single tube) and bitubal (two tubes with one placed concentrically inside the other), empty and filled steel profiles with different materials, dimensions and cross- sectional shapes to study the effects of different tube and filler arrangements on their crushing behaviour. Aluminium foam, produced by a powder metallurgical production process, was applied as filler material. The test results confirmed that considerable mass efficiency improvements with respect to energy absorption could be obtained, even if reduced stroke lengths, caused by the presence of foam, were taken into account. Figure 2.30 shows progressive buckling, i.e. the sequential formation of adjacent local folding patterns of the different specimens. Distinct differences were pointed out between the different cross-sectional shapes. Figure 2.31 shows typical deformed specimens filled tubular crush elements with varying cross sectional shapes (square, hexagonal and octagonal). Bitubal arrangements, consisting of outer and inner profiles with foam in between, were shown to be particularly efficient crush elements, as long as global failure (Euler buckling) could be avoided.

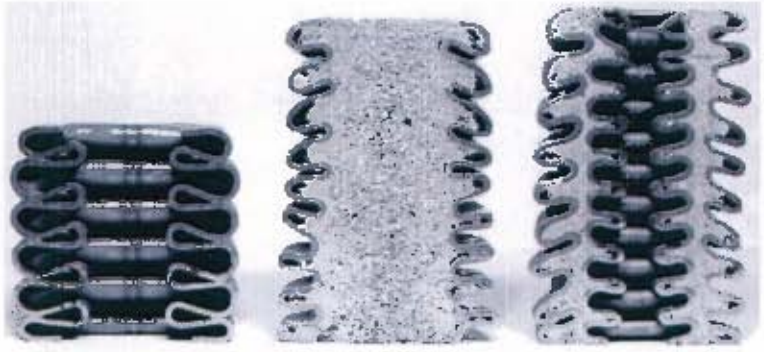

Figure 2.30 : Empty, monotubal filled and bitubal square crushed specimens[102].

Figure 2.31 : Square, hexagonal and octagonal monotubal crushed specimens[102].

Ku *et al.*[103] evaluated the effect of intermittent weldment of cylindrical empty and foam-filled tubes on the energy absorbing behavior under axial crushing. The weld condition did not affect the buckling behaviour of the thin-walled empty tubes showing both irregular diamond folding and regular concertina folding. However, the continuous rupture of the intermittently tack-welded weldment of cylindrical foam-filled tube was found to improve the energy-absorbing capability more than the fully welded one by increasing the load efficiency and decreasing the load amplitude while maintaining the mean crush load energy absorption at a similar level. Even if the buckling mode and folding length were the same, the energy-absorbing efficiency was changed by the variation of the welding pitch.

The influence of high-density foam or pine wood filler on the mode of collapse of quasi-statically and dynamically crushed square metal tubes was investigated by Reddy and Al-Hassani[104]. It was found that the presence of filler reduced the wavelength of axially crushed square metal tubes and different modes of collapse were encountered due to the anisotropy of wood. Thinner tubes buckled in Euler mode when loaded in the direction of the grain of the filling wood.

Singace[105] investigated the influence of foam-like wood filler on the mode of collapse and energy absorption performance of polyvinylchloride (PVC) under quasi-static loading conditions. The mode of collapse of axially crushed PVC tubes was found to revert from regular three-lobe diamond mode to axi-symmetric concertina

mode at a certain wood-filling density. The energy absorption capacity of the PVC tubes was enhanced by wood compression as well as by extra stretching in the tube circumference due to shifting from multi-lobe to axi-symmetric mode. The PVC tubes were visco-elastic in nature and hence would recover some of their length when unloaded. This is clearly exhibited in the cavities shown in Figure 2.32 as a result of recovery after some time from unloading.

Figure 2.32 : Photographs of sectional front and back views of crushed PVC tubes filled with mixed wood sawdust [105].

Zhao et al.[106-108] have also carried out studies on filled tubes. The latter performed quasi-static tests on concrete filled double-skin tubes with different configurations, namely square tubes as both inner and outer, circular tubes as both inner and outer and circular tube as outer tube with an inner square tube. It was found that there is an increase in ductility for concrete filled double-skin tubes in compression when compared to empty single skin tubes. The main conclusions drawn from these studies that concrete filling enhances strength, ductility and energy absorption of the hollow tube, particularly for higher diameter-to-thickness ratio (D_r/H) ratios. This is due to confinement of the core concrete and restraining the steel tube jacket against local buckling.

2.1.4.8 Wrapped tubes

The axial crushing behaviour of wrapped tubes has also been examined. Previous work on the axial crushing of fibre-reinforced-plastic composite tubes has indicated that significant specific energy absorption can be obtained from these materials. Under some circumstances this specific energy exceeds the ones that can be obtained from metal tubing, Refs [109-116]. As stated by Schmueser and Wicklie[117], the governing mechanism is extensive micro-cracking development (not plastic deformation), which may be easily controlled depending on many parameters, such as fibre orientation, properties of the constituent materials (matrix and fibres), geometrical dimensions of the tube and strain rate. The use of the composite to guide and constrain the tube deformation in a favourable manner for dissipating energy were first considered by Wang *et al.*[118] Steel tubes wrapped by fibre-reinforced-plastic composite were crushed under static conditions. It was shown that the energy absorption capacity increased with the thickness of the composite and decreased with the reinforcement angle. Hanefi and Werzbicki[119] extended the work by Wang *et al.*[118] by developing a simplified analytical model for the static compression of metal tubes externally wrapped with composite by 90° winding angle (the angle between the axis of the tube and the tangential direction of winding fibre).

Song *et al.*[120] extended the studies carried out by Hanefi and Wierzbicki[119] to include impact loading, assessing the axial impact crushing behaviour and energy absorption efficiency, of glass/epoxy composite externally wrapped circular metal tubes. The inner tube was made from different metals; aluminium LD2Y, Steel 20# and Copper H68 for typical plastic behaviour and aluminium LY12 and LY12CZ for brittle behaviour. The axial crushing performances were very different for the brittle metal and the plastic metal tube. Figure 2.33 shows the typical collapse modes of bare brittle metal and plastic metal tubes. Fragmentation and petalling occurs in brittle tubes, as shown in Figure 2.33(a), whereas ductile folding occurs in plastic metal tubes. More energy is absorbed by the ductile materials in tube compression tests.

Figure 2.33 : Typical collapse modes of bare brittle metal and plastic metal tube [120]
(a) fragmentation mode of a brittle metal tube; (b) concertina (axisymmetric) mode of a plastic metal tube; (c) diamond (asymmetric) mode of a plastic metal tube

Bouchet *et al.*[121, 122] conducted experiments to study both the crushing behaviour and the adhesion of multi-material structures under dynamic compression conditions. Multi-material structures were obtained by wrapping a carbon/epoxy composite around the outside of an aluminium alloy circular tube. Prior to bonding, different surface treatments (i.e. chemicals etching, anodizing and degreasing) were used in order to improve the adhesion between the composite and the aluminium tube. Two geometries of aluminium alloy tubes, allowing a stable crushing mode, were tested. The specific energy absorption values obtained suggest that the influence of surface treatments of multi-material structures was not a significant contribution. For the thinner aluminium alloy tube, with or without the fibre-reinforced plastic composites, a diamond mode is observed irrespective of the surface treatments. The mode changed from a concertina mode (obtained with the thicker aluminium tube without reinforcement) to a diamond mode for the reinforced tubes, irrespective of the surface treatments. As the crushing mode changed, the reinforcement applied onto the aluminium tube decreased the energy absorbing capacities of the structures. On the other hand, the reinforcement applied on the thinner aluminium tube increased the specific energy absorption of a tube.

Shin *et al.*[123] also investigated the energy absorption capability of axial crushed square aluminum/GFRP hybrid tubes. Glass fibre–epoxy composite prepregs were wrapped around an aluminum tube and cured completely in the autoclave. Bonding between composite and aluminum tubes was performed by excess resin extracted from the composite tube during curing process. The hybrid tube with the 90°-ply orientation composite tube showed the best energy absorption capability among all kinds of hybrid tubes. During deformation of the aluminum tube, the composite material prevented the aluminum tube from folding. The failure of the hybrid tube was stable and progressive without any trigger mechanism because the inner aluminium tube could play the role of crack initiator and controller. Figure 2.34 shows photographs of deformation shapes obtained from the axial crush test of the hybrid tube wrapped by the composite material with 1mm thickness.

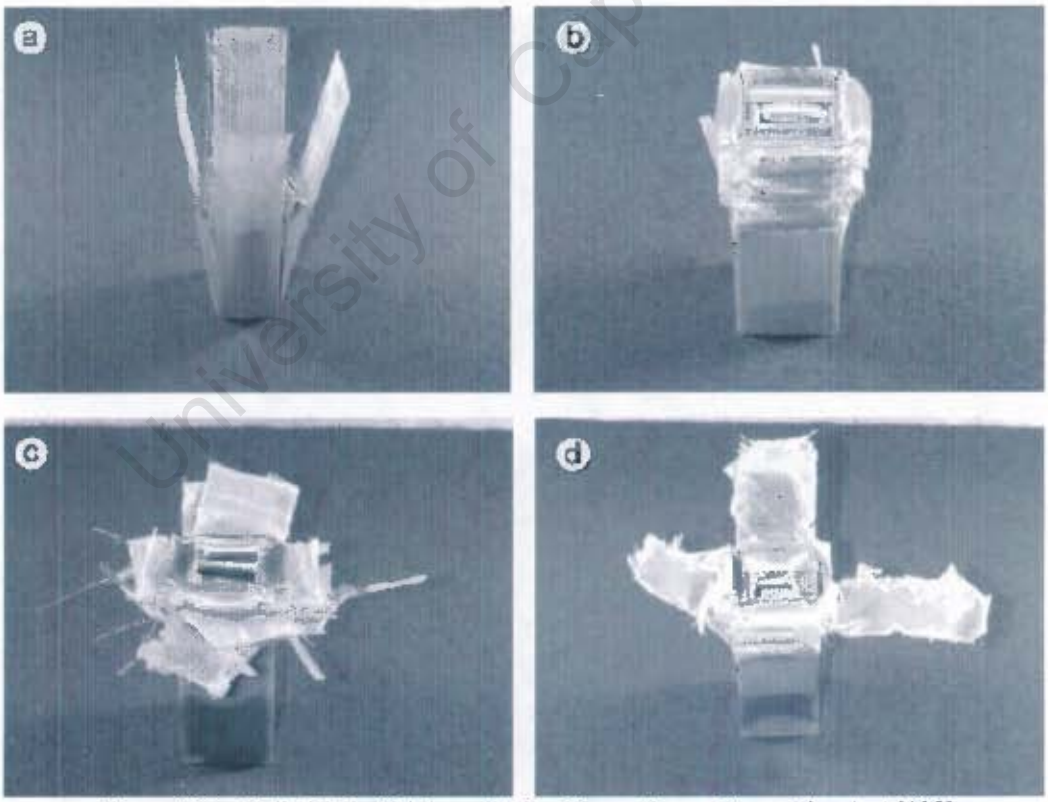

Figure 2.34 : Failed hybrid tubes obtained from the axial crushing test [123]
(a) 0°-ply orientation composite tube, (b) 90°-ply orientation composite tube, (c) 0°/90°-ply orientation composite tube, and (d) +45°-ply orientation composite tube

In summary, results of past studies have shown that tubular structures have the ability to undergo axial crush response. Collapse initiators in combination with end constraints can be used to obtain a particular axial crush mode or modify certain crush characteristics. It can be concluded from existing studies that the response of thin-walled extrusions to axial impact depends on the following:

- Geometry: cross-section, length, width and thickness of the member.
- Material properties: elasticity modulus, yield stress and strain hardening.
- Impact velocity: strain rate and inertia effects.
- Boundary conditions: clamped, pinned or free.
- Imperfections: amplitude, shape and locations.
- Filler: none, aluminium foam, wood (densities).

2.2 Theoretical analysis

Theoretical models of the response of tubes under axial loads far outnumber experimental studies. Simple closed-form solutions can often provide a rapid and sufficiently accurate estimate of, for example, crushing distance and mean crushing load. The crushing behaviour of thin-walled square tubes, because of the geometry, is more complicated than in the case of cylindrical tubes. The details of the analysis are more complex, as anticipated from the photograph of axially crushed square tube shown in Figure 2.35. Wierzbicki and Abramowicz[27] identified and developed two basic collapse elements, type I and type II, shown in Figure 2.36.

Figure 2.35 : Axially crushed square tube (symmetric crushing mode)

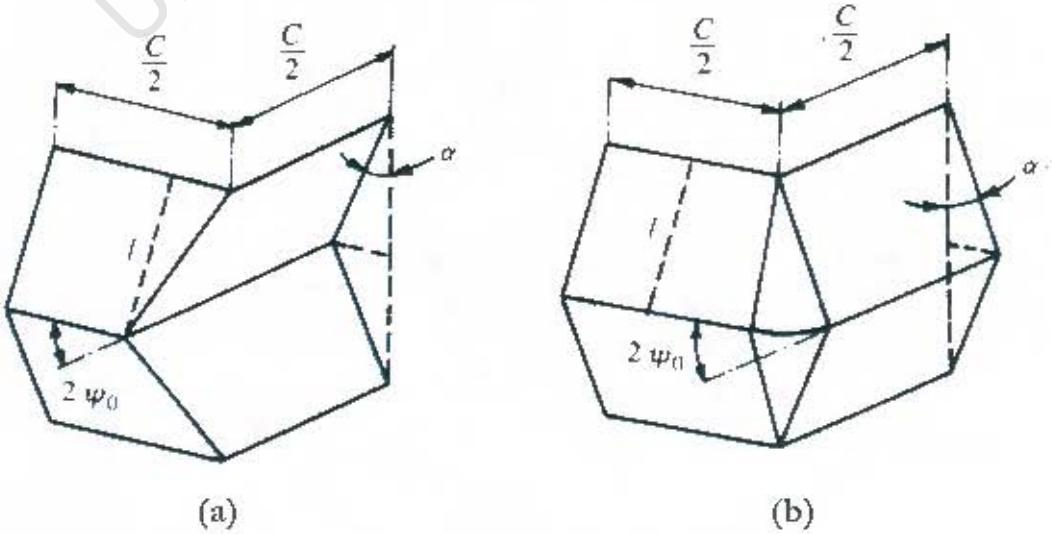

(a) (b)

Figure 2.36 : Basic collapse elements. (a) Type I (b) Type II[27].

These basic collapse elements are used to examine and study both the static and dynamic progressive buckling of square tubes with a mean width C and a mean thickness H. Using these two basic collapse elements, the four possible progressive buckling collapse modes, described in section 2.1.1.2, are constructed. The different modes are created from these elements by either having one layer with four of these elements, or two layers with eight elements in the analysis.

The symmetric crushing mode as shown in Figure 2.35 is idealised with four basic type I collapse elements for each layer of lobes. This crushing mode is predicted to form in thin square tubes with width to thickness ratio greater than 40.8 ($C/H > 40.8$)[28]. In the extensional mode of crushing, each layer of lobes is idealised with four basic type II collapse elements. This type of progressive buckling (shown in Figure 2.35) is predicted in thick square tubes with width to wall thickness ratio less than 7.5 ($C/H < 40.8$)[28].

The asymmetric mixed collapse mode B-type progressive buckling is idealised as two adjacent layers of lobes with seven of the basic collapse type I elements and one of the basic collapse type II element. This type of progressive buckling is predicted to develop within the range $7.5 \leq C/H \leq 40.8$[28]. The difference between the theoretical buckling forces associated with symmetric or asymmetric B mode of failure is small. Therefore, either mode of failure may develop in a square tube with slight imperfections. The asymmetric mixed collapse mode A-type progressive buckling is idealised as two nearby layers of lobes with six basic collapse type I elements and two type II basic collapse elements. The other possible mode of failure is extensional crushing mode. The latter has a slightly higher collapse force than the other three modes but was nonetheless observed by Jones and Abramowicz[7].

2.2.1 Buckling load

2.2.1.1 The mean static buckling load

The mean buckling load is very important from an energy absorption viewpoint. It is used to approximate the total energy that a tube would absorb if the whole length of the tube is completely crushed. Empirical relations were initially developed for use as design tools[5, 6]. More rigorous analyses were later performed to predict the actual mean loads by Abramowicz *et al.*[7-9, 124, 125].

Traditionally, in analytical predictions of mean crushing load, it is assumed that one lobe forms completely before any buckling begins in the next lobe[7-9, 27, 68]. This assumption has been recently modified by Wierzbicki *et al.*[124] to consist of a double folding wave being the active crumpling zone at any instant. The mean force is then calculated by equating the external work done by a nominal force acting over the crushing distance to the internal energy dissipated due to plastic bending and extension.

Symmetric mode

Abramowicz and Jones[7] idealised the symmetric collapse mode for a square tube with thickness H with four type I elements which form one complete layer of lobes. The internal energy consumed by the four basic collapse elements is equated to the external work by the mean axial crushing force. The internal energy is then minimise with respect to b (radius of toroidal shell element) and l (half initial distance between plastic hinges at top and bottom of a basic folding element) to express the mean static crushing load (P_m) as:

$$\frac{P_m}{M_o} = 38.12\left(\frac{C}{H}\right)^{\frac{1}{3}} \tag{2.1}$$

with

$$\frac{l}{H} = 0.99\left(\frac{C}{H}\right)^{\frac{2}{3}} \tag{2.2}$$

and $$\frac{b}{H} = 0.72\left(\frac{C}{H}\right)^{\frac{1}{3}} \quad (2.3)$$

where $$M_o = \frac{\sigma_y H^2}{4} \quad (2.4)$$

Asymmetric mixed collapse mode A

Abramowicz and Jones[7] also idealised the asymmetric mixed deformation mode A with two layers of a total initial height $4l$ and six type I and two type II basic folding elements. Thus, equating the internal energy absorption ($6E_1 + 2E_2$) to the external work ($P_m 4l$) gives the mean static crushing load (P_m) as:

$$\frac{P_m}{M_o} = 33.05\left(\frac{C}{H}\right)^{\frac{1}{3}} + 2.44\left(\frac{C}{H}\right)^{\frac{2}{3}} + \frac{\pi}{2} \quad (2.5)$$

with $$\frac{l}{H} = 0.78\left(\frac{C}{H}\right)^{\frac{2}{3}} \quad (2.6)$$

and $$\frac{b}{H} = 0.63\left(\frac{C}{H}\right)^{\frac{1}{3}} \quad (2.7)$$

Assuming l and b are the same for the symmetric and asymmetric layers present in the deformation mode.

Asymmetric mixed collapse mode B

The asymmetric mixed deformation mode B, according to Abramowicz and Jones[7], consists of two layers with a total initial height of $4l$ and seven type I and one type II basic collapse elements. Thus, equating the internal energy absorption ($7E_1 + E_2$) to the external work ($P_m 4l$) gives the mean crushing load (P_m) as:

$$\frac{P_m}{M_o} = 35.34\left(\frac{C}{H}\right)^{\frac{1}{3}} + 1.35\left(\frac{C}{H}\right)^{\frac{2}{3}} + \frac{\pi}{4} \quad (2.8)$$

with $$\frac{l}{H} = 0.86\left(\frac{C}{H}\right)^{\frac{2}{3}} \quad (2.9)$$

and $$\frac{b}{H} = 0.67\left(\frac{C}{H}\right)^{\frac{1}{3}} \quad (2.10)$$

Extensional collapse mode

Abramowicz and Jones[7] assumed that the extensional collapse mode consisted of one layer with four type II basic collapse elements. Thus, equating the internal energy ($4E_2$) to the external work ($P_m 2l$), gives the mean crushing load (P_m) as:

$$\frac{P_m}{M_o} = 8\pi\left(\frac{C}{H}\right)^{\frac{1}{2}} + 2\pi \tag{2.11}$$

with

$$\frac{l}{H} = \left(\frac{C}{H}\right)^{\frac{1}{2}} \tag{2.12}$$

2.2.1.2 Effective crushing distance

It can be seen from Figure 2.35 that the lobes do not flatten completely during crushing as is idealised in the theoretical analysis leading up to equation 2.1. Abramowicz and Jones[7] showed that the effective crushing distance for symmetric collapse mode is given by:

$$\frac{\delta_1}{2l} = 0.73 \tag{2.13}$$

and for both asymmetric mixed collapse modes and the extensional mode is given by:

$$\frac{\delta_e}{2l} = 0.77 \tag{2.14}$$

Thus assuming,

$$\overline{P}_m \delta_1 = P_m 2l \tag{2.15}$$

Using equations 2.1 and 2.13, a dimensionless mean crushing load of

$$\frac{\overline{P}_m}{M_o} = 52.22\left(\frac{C}{H}\right)^{\frac{1}{3}} \tag{2.16}$$

is obtained for a square tube with symmetric mode of deformation.

Similarly assuming,

$$\overline{P}_m \delta_e = P_m 2l \tag{2.17}$$

and equating 2.5, 2.8, 2.11, and 2.14, dimensionless mean crushing loads of

$$\frac{\overline{P}_m}{M_o} = 42.92\left(\frac{C}{H}\right)^{\frac{1}{3}} + 3.17\left(\frac{C}{H}\right)^{\frac{2}{3}} + 2.04 \tag{2.18}$$

and

$$\frac{\overline{P}_m}{M_o} = 45.90\left(\frac{C}{H}\right)^{\frac{1}{3}} + 1.75\left(\frac{C}{H}\right)^{\frac{2}{3}} + 1.02 \tag{2.19}$$

are obtained for the asymmetric mixed collapse mode A and B respectively, and

$$\frac{\overline{P}_m}{M_o} = 32.64\left(\frac{C}{H}\right)^{\frac{1}{2}} + 8.16 \tag{2.20}$$

for a square tube with an extensional collapse mode.

2.2.1.3 The mean dynamic buckling load

The dynamic progressive buckling of square tubes is idealised as a quasi-static response. In consequence, the equations 2.16, 2.18 and 2.19 predict the dynamic axial crushing force of a thin-walled square tube made from strain rate insensitive material.

Cowper and Symonds[126] suggested a uni-axial constitutive equation relating the dynamic flow stress to the strain rate and the static flow stress as follows:

$$\frac{\sigma'_y}{\sigma_y} = 1 + \left(\frac{\dot{\varepsilon}}{\dot{\varepsilon}_o}\right)^{1/\eta} \tag{2.21}$$

where σ'_y : Dynamic yield stress; σ_y : Static yield stress; $\dot{\varepsilon}$: Strain rate; $\dot{\varepsilon}_o$ and η are material constants. $\dot{\varepsilon}_o = 40.4\ s^{-1}$ and $\eta = 5$ are common, well-known and used values for mild steel[44].

It is interesting to note that when $\dot{\varepsilon} = \dot{\varepsilon}_o$, regardless of the value of η, $\sigma'_y = 2\sigma_y$. Thus, for mild steel, the dynamic flow stress is double the static yield stress at a strain rate of $40.4s^{-1}$. In the case of aluminium, a strain rate of $6500s^{-1}$ is needed to double the flow stress. In consequence, aluminium is often treated as a strain rate insensitive material.

For dynamic axial crushing of square tubes, the equations in section 2.2.1.1 for static crushing need to be modified.

Given the fact that $\sigma = \frac{F}{A}$, and the cross sectional area is assumed to be constant during progressive buckling, the mean dynamic crushing load can be related to the mean static crushing load by the following:

$$\frac{P'_m}{P_m} = 1 + \left(\frac{\dot{\varepsilon}}{\dot{\varepsilon}_o}\right)^{1/\eta} \tag{2.22}$$

Equation 2.16 thus becomes

$$\frac{P'_m}{M_o} = 52.22\left(\frac{C}{H}\right)^{\frac{1}{3}}\left\{1 + \left(\frac{\dot{\varepsilon}}{\dot{\varepsilon}_o}\right)^{1/\eta}\right\} \tag{2.23}$$

for symmetric mode of progressive buckling. It is difficult to predict the strain rate, $\dot{\varepsilon}$, in a square tube because of its complex deformation patterns when the tube undergoes progressive buckling. Abramowicz and Jones[7] derived the following expression for the average strain rate in square tubes as:

$$\dot{\varepsilon} = \frac{Hv_m}{2b_f\delta_t} \tag{2.24}$$

where : mean velocity, $v_m = v/2$, v : impact velocity of striking mass;

δ_t : effective crushing distance; b_f : radius of toroidal shell element

The rolling radius associated with the toroidal deformation surface varies during progressive crushing. While equations 2.3, 2.7, 2.10 give the mean rolling radius, the final value of the rolling radius is used to estimate the average strain rate.

For square tubes collapsing in the symmetric mode;

The final rolling radius is given by:

$$\frac{b_f}{l} = 0.53\left(\frac{C}{H}\right)^{\frac{1}{3}} \tag{2.25}$$

Mean strain rate becomes:

$$\dot{\varepsilon} = 0.33\frac{v_o}{C} \tag{2.26}$$

And hence, mean dynamic crushing load:

$$\frac{P'_m}{M_o} = 52.22\left(\frac{C}{H}\right)^{\frac{1}{3}}\left\{1+\left(\frac{0.33v_o}{C\dot{\varepsilon}_o}\right)^{1/\eta}\right\} \tag{2.27}$$

For square tubes collapsing in the asymmetric mixed mode A

The final rolling radius is given by:

$$\frac{b_f}{l} = 0.45\left(\frac{C}{H}\right)^{\frac{1}{3}} \tag{2.28}$$

Mean strain rate becomes:

$$\dot{\varepsilon} = 0.49\frac{v_o}{C} \tag{2.29}$$

And hence, mean dynamic crushing load:

$$\frac{P'_m}{M_o} = \left\{43.61\left(\frac{C}{H}\right)^{\frac{1}{3}} + 3.79\left(\frac{C}{H}\right)^{\frac{2}{3}} + 2.6\right\}\left\{1+\left(\frac{0.49v_o}{C\dot{\varepsilon}_o}\right)^{1/\eta}\right\} \tag{2.30}$$

For square tubes collapsing in the asymmetric mixed mode B

The final rolling radius is given by:

$$\frac{b_f}{l} = 0.48\left(\frac{C}{H}\right)^{\frac{1}{3}} \tag{2.31}$$

Mean strain rate becomes:

$$\dot{\varepsilon} = 0.41\frac{v_o}{C} \tag{2.32}$$

And hence, mean dynamic crushing load:

$$\frac{P'_m}{M_o} = \left\{ 46.16\left(\frac{C}{H}\right)^{\frac{1}{3}} + 2.14\left(\frac{C}{H}\right)^{\frac{2}{3}} + 1.3 \right\} \left\{ 1 + \left(\frac{0.41 v_o}{C\dot{\varepsilon}_o} \right)^{1/\eta} \right\} \quad (2.33)$$

2.2.1.4 Ultimate buckling load

The ultimate buckling load for tubes failing by either static or dynamic progressive buckling is greater than the subsequent peak loads forming the subsequent lobes. The ultimate load is governed by elastic-plastic buckling and can be approximated by:

$$P_{ult} = \sigma_o A \quad (2.34)$$

where σ_o: plastic flow stress; A : cross sectional area of the tube.

Wierzbicki and Abramovicz[127] found that the flow stress, σ_o, could be approximated as 92% of the ultimate tensile stress. Surko[56] used the von Karman postulate to define the plastic flow stress as:

$$\sigma_o = \frac{2\alpha\sigma_y H}{C} \quad (2.35)$$

where α is a material constant defined by:

$$\alpha^2 = \frac{\pi^2 E}{12(1-\nu^2)\sigma_y} \quad (2.36)$$

2.2.2 Energy absorption of the structures

The impact-energy performance of tubular sections can be specified in many ways to accommodate its wide range of applications. The total energy absorbed by the structure through elastic and plastic work calculated as work done is given by equation 2.37.

$$E_{absorbed} = \int_0^{\delta} F(u).du \tag{2.37}$$

where F(u) is the crushing force as a function of crush distance in the axial direction

This quantity is represented as the area under the axial force-displacement curve. Numerical integration using the trapezium scheme as presented in equation 2.38 can be used to calculate this absorbed energy based on the axial force-displacement curve.

$$E_{absorbed} = \frac{1}{2}\sum_{i}^{n-1}(F(u)_{i+1} + F(u)_i).(u_{i+1} - u_i) \tag{2.38}$$

The resulting mean crushing load is therefore given by equation 2.39

$$P_m = \frac{E_{absorbed}}{\delta} \tag{2.39}$$

Many dimensionless collapse efficiency parameters have been introduced to compare the effectiveness of energy absorbers of different shapes, sizes and materials [44, 97]. Some of these parameters are also defined by Mahmood and Paluzsny (cited by [70]).

2.2.2.1 Geometric efficiency, e_G

The geometric efficiency, e_G (cited by [70]), also referred to as stroke efficiency, is a measure of how well the absorber is compressed and is given by equation 2.40 as the ratio of crushed distance to original length. The geometric efficiency parameter is, however, dependent on the initial kinetic energy.

$$e_G = \frac{\delta}{L} \tag{2.40}$$

2.2.2.2 Load efficiency, e_L

The load efficiency, e_L (cited by [70]), also referred to as force efficiency, is given by equation 2.41. It is a measure of load fluctuations that occur during the crushing of the structure.

$$e_L = \frac{P_m}{P_{MAX}} \tag{2.41}$$

2.2.2.3 Energy efficiency, e_E

A more comprehensive collapse efficiency parameter is the energy efficiency, e_E (cited by [70]), which is defined as the ratio of energy absorbed to the theoretical maximum energy that can be absorbed. It is equivalent to the load efficiency and is given by equation 2.42.

$$e_E = \frac{E_{absorbed}}{P_{MAX}.\delta} \tag{2.42}$$

2.2.2.4 Specific energy, S_e

Another measure of efficiency is the specific energy, S_e [44], which is defined as the energy absorbed per unit mass. This useful parameter provides a method of comparing energy absorbing structures with different masses and is given by equation 2.43.

$$S_e = \frac{E_{absorbed}}{m} \tag{2.43}$$

For a thin-walled tube with a square cross-section, equation 2.43 can be re-written to the form in equation 2.44.

$$S_e = \frac{P_m \delta}{4CHL\rho} \tag{2.44}$$

2.3 Computational predictions

In spite of the numerous studies on both the static and dynamic response of tubes, according to Karagiozova and Jones[128], there has been no clear classification on the influence of various parameters, such as geometries, loading conditions and material properties, which cause the development of different dynamic buckling phenomena. Finite Element analysis has been widely applied to analyse the crushing of tubes, enabling parameters and boundary conditions which are not accessible experimentally or analytically to be investigated. Consequently, this numerical tool has become an ideal instrument to gain a better understanding of the failure mechanism of the extrusions under compressive loading conditions.

The different shell response characteristics, such as peak load, fold length, axial compression and energy absorption have been studied using the numerous finite element techniques available. A few examples of the different Finite element codes used to investigate these characteristics include the work of Langseth *et al.*[54, 129], Otubushin[130] and Marsolek and Reimerdes[131] who used LS-DYNA. Abah *et al.*[57] and Markiewicz[132] used PAM-CRASH. Miyazaki *et al.*[133] used the Finite Element package, MARC K6.2. Nannucci *et al.*[36] and Karagiozova *et al.*[134-137] used ABAQUS. In most of the studies, an explicit integration scheme was used. 4-noded shell elements with reduced integration, multiple integration points through the thickness of the element and hourglass control were used.

Mamalis *et al.*[138], however, used an "implicit" finite element code, MARC, to simulate the crush behaviour of cylindrical thin-wall composite tubes under static and dynamic axial compression, in accordance with the progressive mechanism of failure. The predicted numerical results were validated by comparing with actual experimental data obtained from quasi-static and impact tests conducted in a tensile test machine and a drop hammer rig respectively.

Tubular structures, irrespective of cross-sections, can absorb a considerable proportion of the initial kinetic energy during the initial phase of axial compression. The numerical simulation of the tube response in Karagiozova *et al.*[48] revealed that a high peak load developed when a shell was subjected to high-velocity impacts. Such a peak load was also observed experimentally. However a limited number of results were available because of measurement difficulties[21]. Usually, the experimental data was filtered at relatively low frequencies, which caused a delay in the first peak load at the beginning of the impact event. The filtered data could also affect the magnitude of the peak force.

A study of the peak load was reported by Kurokawa *et al.*[139] who compared experimental data with a numerical simulation for a high-velocity mass impact of a cylindrical shell. It was suggested that a uni-axial stress state developed in the shell at the beginning of impact due to the restraint of radial inertia effects that were associated with high velocity impacts. However, an unrealistic time of 0.5 μs for the development and duration of the peak load was reported. It was found in Karagiozova *et al.*[48], that the peak loads acted during a time of about 65μs, which was comparable with the time necessary to develop a single wrinkle in a shell.

While most analyses were concerned mainly with the variation of the shell geometry and the loading conditions a few studies have examined the influence of material properties on the dynamic shell response according to Reid[140]. The influence of the material models, with respect to temperature effects at high strain rates, on the prediction of the response of aluminium alloy circular and square tubes was discussed by Karagiozova *et al.*[141]. The analysis showed that the material properties played an important role in the formation of the buckling pattern due to the finite duration of the initial compression phase when plastic stress waves propagated along a shell at different speeds. However, the temperature effect did not appear to affect the energy absorbing characteristics of the shell, but nevertheless could cause a local tearing of a wrinkle due to the hugely localised plastic strains. Figure 2.37 shows